

1 **How wavelength affects hydrodynamic performance of two accelerating**
2 **mirror-symmetric undulating hydrofoils**

3 Zhonglu Lin (林中路),^{1,2,3} Dongfang Liang (梁东方),² Amneet Pal Singh Bhalla,⁴
4 Ahmed A. Sheikh Al-Shabab,⁵ Martin Skote,⁵ Wei Zheng (郑炜),^{1,6,7,3} and Yu Zhang
5 (张宇)^{1,3}

6 ¹⁾*Key Laboratory of Underwater Acoustic Communication and Marine Information*
7 *Technology of the Ministry of Education, College of Ocean and Earth Sciences,*
8 *Xiamen University, Xiamen City, Fujian Province, 361005,*
9 *China*

10 ²⁾*Engineering Department, University of Cambridge, Cambridge City, Cambridgeshire,*
11 *CB2 1PZ, United Kingdom*

12 ³⁾*State Key Laboratory of Marine Environmental Science, College of Ocean*
13 *and Earth Sciences, Xiamen University, Xiamen City, Fujian Province, 361005,*
14 *China*

15 ⁴⁾*Department of Mechanical Engineering, San Diego State University, San Diego City,*
16 *California State, 92182-1323, United States*

17 ⁵⁾*School of Aerospace, Transport and Manufacturing, Cranfield University, Cranfield City,*
18 *Bedfordshire, MK43 0AL, United Kingdom*

19 ⁶⁾*Pen-Tung Sah Institute of Micro-Nano Science and Technology,*
20 *Xiamen University, Xiamen City, Fujian Province, 361005,*
21 *China*

22 ⁷⁾*Discipline of Intelligent Instrument and Equipment, Xiamen University, Xiamen City,*
23 *Fujian Province, 361005, China*

24 (*Electronic mail: yuzhang@xmu.edu.cn)

25 (Dated: July 4, 2023)

This is the author's peer reviewed, accepted manuscript. However, the online version of record will be different from this version once it has been copyedited and typeset.

PLEASE CITE THIS ARTICLE AS DOI: 10.1063/5.0155661

Accepted to Phys. Fluids 10.1063/5.0155661

26 Fish schools are capable of simultaneous linear acceleration. To reveal the underly-
 27 ing hydrodynamic mechanism, we numerically investigate how Reynolds number $Re =$
 28 $1000 - 2000$, Strouhal number $St = 0.2 - 0.7$ and wavelength $\lambda = 0.5 - 2$ affect the mean
 29 net thrust and net propulsive efficiency of two side-by-side hydrofoils undulating in anti-
 30 phase. In total, 550 cases are simulated using immersed boundary method. The thrust
 31 increases significantly with wavelength and Strouhal number, yet only slightly with the
 32 Reynolds number. We apply a symbolic regression algorithm to formulate this relation-
 33 ship. Furthermore, we find that mirror-symmetric schooling can achieve a *net* thrust more
 34 than ten times that of a single swimmer, especially at low Reynolds numbers. The highest
 35 efficiency is obtained at $St = 0.5$ and $\lambda = 1.2$, where St is consistent with that observed
 36 in the linear-accelerating natural swimmers, e.g. Crevalle jack. Six distinct flow structures
 37 are identified. The highest thrust corresponds to an asymmetric flow pattern, whereas the
 38 highest efficiency occurs when the flow is symmetric with converging vortex streets.

39 I. INTRODUCTION

40 A. Background overview

41 Fish swimming have been extensively studied for decades in various disciplines, e.g. morphol-
 42 ogy (Webb, 1984), animal behaviour (Ashraf *et al.*, 2017), robotics (Li *et al.*, 2020) and especially
 43 hydrodynamics (Weihs, 1973; Borazjani and Sotiropoulos, 2010; Dong and Lu, 2007; Maertens,
 44 Triantafyllou, and Yue, 2015; Maertens, Gao, and Triantafyllou, 2017; Pan and Dong, 2020;
 45 Chao *et al.*, 2019; Chao, Alam, and Ji, 2021). The investigation of fish swimming mechanisms
 46 can inspire the next-generation biomimetic design of autonomous underwater vehicles (AUVs),
 47 as the locomotive performance of commercially available AUVs is yet to match those of natural
 48 swimmers (Fish, 2020). The present research focuses on the effects of wavelength on two undulat-
 49 ing NACA0012 hydrofoils swimming side-by-side. The results can help understand the underlying
 50 mechanism of accelerated fish schools. Simultaneous acceleration of fish school can frequently
 51 occur in nature (Partridge, 1981) to evade predators (Zheng *et al.*, 2005; Deng and Liu, 2021) or to
 52 conduct collective manoeuvre (Lecheval *et al.*, 2018) using vision (Rosenthal *et al.*, 2015), lateral
 53 line (Coombs and Montgomery, 2014) and proprioceptive sensing (Li *et al.*, 2021a). Although the
 54 effects of wavelength have been investigated in the context of a single swimmer (Thekkethil *et al.*,
 55 2017; Khalid *et al.*, 2021; Chao, Alam, and Cheng, 2022), it remains an open question as to how
 56 wavelength kinematics affect accelerating fish schools. The following reviews on fish swimming
 57 studies regarding the wavelength effect, acceleration, and side-by-side fish schooling highlight the
 58 research gap that can be filled by the present study.

59 In nature, the swimming body wavelength is not only different across various species with
 60 different swimming styles at steady swimming (Santo *et al.*, 2021), but also varies with the loco-
 61 motion phase of a single swimmer (Du Clos *et al.*, 2019), e.g. starting from rest, linear acceleration
 62 and steady swimming. Santo *et al.* (2021) recently conducted a comparative study on the kinemat-
 63 ics of 44 body-caudal fin (BCF) fish species, focusing on the steady swimming phase. Santo *et al.*
 64 (2021) summarised and compared the wavelengths of different BCF species, considering the four
 65 classic swimming styles of *anguilliform*, *subcarangiform*, *carangiform* and *thunniform*. The me-
 66 dian wavelength significantly increased from *anguilliform* (0.75 body length) to *thunniform* (1.14
 67 body length), yet the wavelength for the tested species occupies a broad range from 0.5 body length
 68 to 1.5 body length. For conciseness, we abbreviate "body length" as "BL" in the following content.

The wavelength of four swimming styles overlaps from 0.75BL to 1.35BL, indicating this wavelength range may be compatible with swimmers of various body shapes and swimmers of different swimming styles. The results by Santo *et al.* (2021) have driven us to focus on a similar range of wavelengths, which will be presented later in Section II A. Du Clos *et al.* (2019) studied how an *anguilliform* swimmer accelerates from rest, and compared the kinematics during steady swimming and acceleration. They discovered that the wavelength during escape acceleration $\lambda \approx 2$, much longer than that during steady swimming with $\lambda = 0.8$. Nangia *et al.* (2017a) conducted a meta-analysis regarding the wavelength and Strouhal number for various BCF species, finding a convergence of the ratio of wavelength to the tail amplitude during undulation. Nangia *et al.* (2017a) utilised the ConstraintIB module of open-source immersed boundary software, IBAMR, which is also used in our present study.

B. Wavelength effects for a single swimmer during steady-swimming and linear acceleration

Many numerical studies focused on the wavelength effect of a single swimmer, both in 2D and 3D. Chao, Alam, and Cheng (2022) recently conducted a thorough investigation of the hydrodynamic performance of a single slender swimmer with various Strouhal numbers $St = 0.1 - 1$, Reynolds number $Re = 50 - 2000$, and $\lambda = 0.5 - 2$, and they discovered seven types of wake structures. They were able to condense the simulation results into a few formulas. Their study has inspired the present study's choice of parametric space. Khalid *et al.* (2020) studied how a single tethered undulating 2D NACA0012 hydrofoil performs with either *anguilliform* or *carangiform* kinematics in a parametric sweep of $Re = 100, 1000, 5000$, $St = 0.1 - 0.8$, and $\lambda = 0.5 - 1.5$. They found that wavelengths do not necessarily optimise the hydrodynamic performance of natural swimmers. Thekkethil *et al.* (2017), Thekkethil, Sharma, and Agrawal (2018, 2020) and Gupta *et al.* (2021) conducted a series of studies regarding how the wavelength affects the thrust and propulsive efficiency of a single undulating NACA0012 hydrofoil. Khalid *et al.* (2021) conducted high fidelity 3D simulations of a steady-swimming American eel at $St = 0.3 - 0.4$, investigating the influences of wavelengths at $\lambda = 0.65 - 1.25$. They found that short wavelengths are more hydrodynamically advantageous for *anguilliform* swimmers during their steady motion. Borazjani and Sotiropoulos (2008, 2009) conducted a 3D simulation to study a steady-swimming *carangi-*

99 *form* (Borazjani and Sotiropoulos, 2008) and an *anguilliform* (Borazjani and Sotiropoulos, 2009)
 100 swimmer tethered in a free stream flow at $Re = 300, 4000$, whereas the wavelength is configured
 101 at $\lambda = 0.642 - 1.1$.

102 In addition, in the present paper, we apply 2D model rather than 3D considering computational
 103 cost to simulate 550 cases. What is more, 2D simulation has proven to reveal fundamental patterns
 104 in undulating hydrofoils with various wavelengths in the laminar flow regime (Chao, Alam, and
 105 Cheng, 2022).

106 The above-mentioned studies have focused on the steady swimming phase. However, steady-
 107 swimming is a rare scenario for fish swimming. Other conditions include the starting from rest
 108 (Domenici and Hale, 2019) and the linear acceleration (Akanyeti *et al.*, 2017). The linear acceler-
 109 ation occurs when they travel or hold a position in a variable speed or turbulent flow Tytell (2004).
 110 While steady-swimming and fast-start (Eaton, Bombardieri, and Meyer, 1977; Tytell and Lauder,
 111 2008; Borazjani *et al.*, 2012; Borazjani, 2013) are relatively well studied, linear acceleration is
 112 still not well understood in both biological and hydrodynamic aspects for a single swimmer, let
 113 alone for fish schools.

114 Wavelength correlates significantly with acceleration and speed during the linear acceleration
 115 phase of fish swimming. The existing biological research almost all focused on a *single* acceler-
 116 ating fish. An overview of the wavelength and swimming styles is depicted in Fig. 1. Schwalbe
 117 *et al.* (2019) scrutinised the function of red muscle, i.e. slow-twitch muscle for sustained activ-
 118 ities, during the acceleration of bluegill sunfish *Lepomis macrochirus* and how it affects the fish
 119 kinematics. They discovered that the fish's undulation kinematics during acceleration differs from
 120 that during steady swimming. Body wavelength decreases significantly during acceleration, yet in-
 121 creases significantly with swimming speed. Their research focused on the bluegill sunfish *Lepomis*
 122 *macrochirus*. At different acceleration levels, the fish body wavelength can range from 0.75BL to
 123 0.9BL. They focused on the fish muscle activation and observation of kinematics. Akanyeti *et al.*
 124 (2017) conducted both biological and robotic fish experiments to investigate the kinematic char-
 125 acteristics and hydrodynamic performance during linear acceleration. Their investigation was car-
 126 ried out using a *tethered* robotic fish while varying the free stream flow to study the *acceleration*
 127 at consecutive instants. Our present problem setup is similar to their experimental configuration.
 128 They found that tail-beat frequency, rather than amplitude, is most effective on swimming speed
 129 and acceleration. The tail-beat amplitude remains constant during steady swimming or accelera-
 130 tion. Hence, our present study fixes tail-beat amplitude while varying the Strouhal number. Tytell

(2004) conducted the first quantitative research on the linear acceleration of an *anguilliform* swimmer, focusing on its kinematics and wake hydrodynamics. They found that body wavelength λ and tailbeat frequency both significantly increase with steady swimming speed.

C. Side-by-side steady swimming with constant wavelength

Side-by-side fish schooling is relatively well studied, yet most studies have focused on the steady swimming scenario with a fixed wavelength. Ashraf *et al.* (2017) conducted a fish schooling experiment, discovering that fish favours the phalanx formation, i.e. side-by-side of multiple fish, at relatively high steady-swimming speed. The tested Reynolds number ranges from 1000 to 6000. Li *et al.* (2021b) investigated the schooling of two robotic fish of *subcarangiform*, swimming steadily side-by-side with rigid linking between them, with the lateral distance fixed at 0.33BL. For schooling swimmers, they discovered maximum speed and efficiency at in-phase and anti-phase conditions, respectively, which are compared with a single swimmer. In the present paper, we also fix the gap distance at 0.33BL. For side-by-side and anti-phase pitching foils, previous studies reached a consensus that much higher thrust can be produced with efficiency similar to a single swimmer (Dewey *et al.*, 2014; Huera-Huarte, 2018; Gungor and Hemmati, 2021; Yucel, Sahin, and Unal, 2022). Our present paper further investigates the hydrodynamic effects due to various wavelengths. Li *et al.* (2020) conducted a thorough study on a tethered two-fish school at a steady swimming phase, combining robotic fish experiments and biological observation. They discovered that the front-back distance and phase difference most significantly affected schooling performance. The lateral distance varies from 0.27 to 0.33 in this study. Shrivastava *et al.* (2017) conducted a 2D simulation of three hydrofoils swimming side-by-side. Interaction between the swimmers can be observed at a lateral distance less than 1BL with $St = 0.4 - 0.8$, A_{\max} , $\lambda = 1$, $Re = 400$. Wei *et al.* (2022) simulated two initially side-by-side swimmers passively self-propelling with three degrees of freedom. They configured the initial gap ratio as $G = 0.4 - 0.9$, and observed improved schooling performance between the two swimmers. Therefore, the present lateral distance of 0.33BL should allow sufficient schooling interaction between the two swimmers. Gungor, Khalid, and Hemmati (2022) investigated the unsteady hydrodynamics of two pitching foils in side-by-side formation. By drawing wake maps, they discovered three distinct vortex patterns of separated, merged, and transitional-merged wake.

161 D. Present study scope

162 In summary, the above-mentioned literature has inspired us that fish-body wavelength is a key
 163 factor affecting the fluid-structure interaction of fish-like swimmers, yet the research regarding
 164 wavelength-effect on *schooling* and *accelerating* swimmers are relatively scarce, despite its oc-
 165 currence in the nature, e.g. fish school escaping from predator. Also, we use the term "mirror-
 166 symmetric" as an equivalent of "side-by-side and anti-phase", not only for the sake of concise-
 167 ness but also because we would like to strengthen the physically-interesting phenomenon of flow
 168 symmetry and its breaking at certain conditions. More specifically, although excellent studies
 169 have emerged to examine single fish wavelength effects (Santo *et al.*, 2021; Khalid *et al.*, 2021;
 170 Thekkethil, Sharma, and Agrawal, 2020; Du Clos *et al.*, 2019; Nangia *et al.*, 2017a), linear ac-
 171 celeration (Tytell, 2004; Akanyeti *et al.*, 2017; Schwalbe *et al.*, 2019) and side-by-side schooling
 172 (Wei *et al.*, 2022; Li *et al.*, 2021b; Shrivastava *et al.*, 2017; Ashraf *et al.*, 2017), how body
 173 wavelength affects the linear acceleration of two side-by-side fishlike swimmers has never been
 174 systematically investigated. We aim to present a thorough investigation in the present paper, which
 175 can be helpful in understanding the fish schooling behaviour and to design the collective locomo-
 176 tion strategy of underwater fish-like AUVs. The rich physics in side-by-side fish schooling can
 177 also be relevant to the flow mediated interaction between two oscillating cylinders (Lin, Liang,
 178 and Zhao, 2022, 2019, 2018b,a, 2017, 2016; Gazzola *et al.*, 2012; Nair and Kanso, 2007; Lamb,
 179 1932).

This is the author's peer reviewed, accepted manuscript. However, the online version of record will be different from this version once it has been copyedited and typeset.

PLEASE CITE THIS ARTICLE AS DOI: 10.1063/5.0155661

Accepted to Phys. Fluids 10.1063/5.0155661

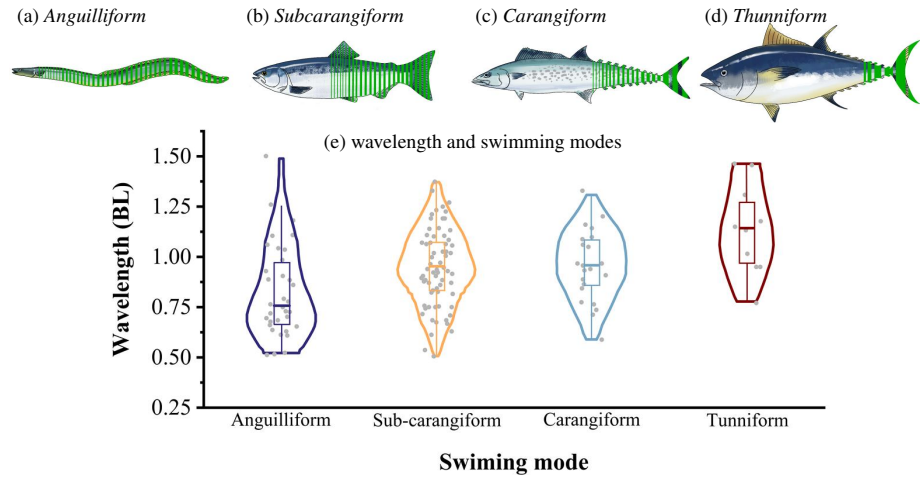


Figure 1. Four different swimming modes of Body-Caudal-Fin type locomotion (a) *Anguilliform* (body undulation, e.g. eel) (b) *Subcarangiform* (body undulation with caudal fin pitching, e.g. salmonid) (c) *Carangiform* (minor body undulation with caudal fin pitching, e.g. makrell) (d) *Thunniform* (mainly caudal fin pitching, e.g. tuna). The shaded area demonstrates the body parts with a significant lateral motion to generate thrust (redrawn from figures by Lindsey (1978) and Sfakiotakis, Lane, and Davies (1999)). (e) distribution of wavelength with the four swimming modes (adapted from figure by Santo *et al.* (2021)): These four types have wavelengths ranging from 0.5 to 2 body length for steady swimming conditions across various fish species regardless of the aforementioned body-caudal fin sub-types.

180 II. METHODOLOGY

181 In this section, we present the methodology of the current study. Section II A describes the
182 representative problem setup accounting for the schooling swimmers, including geometry, kine-
183 matic equation, and non-dimensional analysis. Section II B discusses the computational method
184 to implement the problem setup.

185 A. Problem setup

186 It is not uncommon to observe simplified models relevant to fish swimming, including a trav-
187 elling wavy boundary (Ma, Huang, and Xu, 2019; Wang *et al.*, 2021), filaments (Ni, Huang,
188 and Xu, 2023), and undulating NACA foils (Lin *et al.*, 2023). The present problem setup applies
189 NACA0012 hydrofoil to represent the fish-like swimmer, since the NACA foils have been exten-
190 sively used as a representation in the previous investigations (Deng *et al.*, 2022, 2016, 2015; Shao
191 *et al.*, 2010; Deng, Shao, and Yu, 2007; Yu and Huang, 2021; Pan and Dong, 2022). The complete
192 configuration is summarised in Fig. 2. The accelerated fish schooling problem is represented by
193 a two-dimensional form with two wavy hydrofoils undulating side-by-side. The 2D configuration
194 should adequately describe the present laminar flow regime with $Re \leq 2000$ (Gazzola, Argentina,
195 and Mahadevan, 2014; Chao, Alam, and Cheng, 2022).

196 The fish body is simplified as a 2D NACA0012 hydrofoil to describe bio-propulsion problems
197 with pitching (Morange, Flores, and García-Villalba, 2016) and undulating hydrofoils (Thekkethil
198 *et al.*, 2017). The geometry of a NACA0012 hydrofoil is similar to that of a *carangiform* or
199 *subcarangiform* swimmer. The two foils are placed side-by-side while undulating in anti-phase to
200 concentrate on a limited number of variables typical for fish schooling (Ashraf *et al.*, 2017). The
201 kinematics of the swimmers is described by the travelling wave equations in the non-dimensional
202 form:

$$203 \quad Y_1 = A_{\max} X_1 \sin \left[2\pi \left(\frac{X_1}{\lambda} - \frac{St}{2A_{\max}} t \right) \right] \quad (1)$$

$$204 \quad Y_2 = A_{\max} X_2 \sin \left[2\pi \left(\frac{X_2}{\lambda} - \frac{St}{2A_{\max}} t \right) + \pi \right] \quad (2)$$

206 This is also a common configuration (Thekkethil, Sharma, and Agrawal, 2018), and is cho-
207 sen here for the convenience of comparison. For completeness, the meaning of the variables is

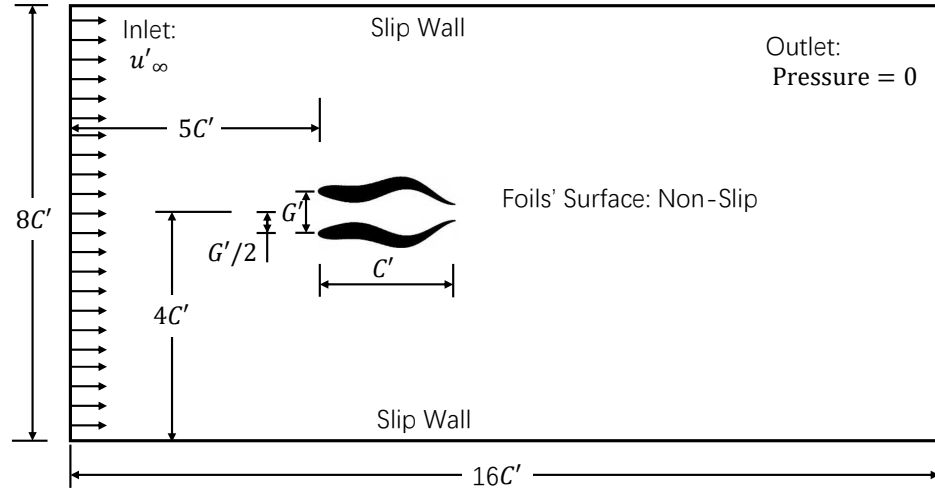


Figure 2. Sketch of the present problem setup: two side-by-side fish swimming in anti-phase with a fixed lateral gap distance $G = 0.33$. The two swimmers are mirror symmetric to each other along the horizontal line $y = 4C$.

208 listed as follows: $Y_i = Y'_i/C'$ is the centre-line lateral displacement of each hydrofoil; $X_i = X'_i/C'$
 209 is the streamwise position on the centreline; $i = 1$ denotes the top swimmer while $i = 2$ repre-
 210 sents the bottom swimmer. $t = t'u'_\infty/C'$ is non-dimensional time; u'_∞ is the free-stream velocity;
 211 $A_{\max} = A'_{\max}/C'$ is non-dimensional tail tip amplitude, where C' is the fish body length; a_{\max} is
 212 the dimensional tail-amplitude; $\lambda = \lambda'/C'$ is non-dimensional wavelength, with λ' being the di-
 213 mensional foil undulating wavelength; $St = 2f'A'_{\max}/u'_\infty$ is Strouhal number, with f' being the
 214 dimensional undulating frequency. Here, dashed alphabets denote dimensional parameters.

215 In addition, non-dimensional groups to describe a particular case are listed in Table 1 together
 216 with the investigated parametric space, in which ρ' is the fluid density; f' is the undulating fre-
 217 quency; μ' is the dynamic viscosity. The non-dimensional lateral and front-back distances are
 218 fixed at $G = G'/C' = 0.33$ and $D = D'/C' = 0$. In summary, only three variables are involved
 219 in the present study: Reynolds number $Re = 1000 - 2000$, Strouhal number $St = 0.2 - 0.7$, and
 220 non-dimensional wavelength $\lambda = 0.5 - 2.0$.

221 The outputted metrics of the swimming performance are listed in Table 2. Thrust is directly rel-
 222 evant to acceleration, whereas net propulsive efficiency measures how efficiently the input energy

is converted to the net thrust for acceleration. The examination of the vorticity field is necessary to examine the flow symmetry and stealth capacity. In Table 2, $F_{T,i}$ is the net thrust on hydrofoils; $C_{L,i}$ is the instantaneous lateral force coefficient; \mathbf{u} is the fluid velocity. ω^* is the non-dimensional vorticity, whereas P^* stands for the non-dimensional pressure.

Table 1. Non-dimensional input parameters and the involved range of value

| | | | |
|-----------------|-----------|-----------------------------|-------------|
| Reynolds number | Re | $\rho' u_\infty' C' / \mu'$ | 1000 – 2000 |
| Strouhal number | St | $2f'A'_{\max}/u'_\infty$ | 0.2 – 0.7 |
| Wavelength | λ | λ'/C' | 0.5 – 2 |

B. Simulation method

The present paper simulates the problem using a customised version of the ConstraintIB module (Bhalla *et al.*, 2013; Griffith and Patankar, 2020) implemented in IBAMR (Griffith, 2013), which is an open-source immersed boundary method simulation software that depends on several underlying advanced libraries including SAMRAI (Hornung and Kohn, 2002; Hornung, Wissink, and Kohn, 2006), PETSc (Balay *et al.*, 1997, 2010, 2001), hypre (Falgout *et al.*, 2010; Balay *et al.*, 1997), and libmesh (Kirk *et al.*, 2006). It is chosen for its adaptive mesh refinement capacity of the Eulerian background mesh, allowing both computational efficiency and adequate accuracy. The ConstraintIB method has been extensively validated (Bhalla *et al.*, 2013; Bhalla, Griffith, and Patankar, 2013; Bhalla *et al.*, 2014; Nangia *et al.*, 2017b; Nangia, Patankar, and Bhalla, 2019; Griffith and Patankar, 2020; Bhalla *et al.*, 2020). The present customised version has also been validated in (Lin *et al.*, 2023). The maximum Reynolds number $Re \leq 2000$ in the present study is lower than that in a previous study (Lin *et al.*, 2023) with $Re = 5000$, so here we adopt the

Table 2. Non-dimensional output parameters for swimming performance

| | | |
|---------------------------------------|-----------------|--|
| Cycle-averaged net thrust coefficient | $\bar{C}_{T,i}$ | $\frac{1}{T} \int_t^{t+T} C_T dt = \frac{1}{T} \int_t^{t+T} 2F_{T,i} / \rho u_\infty^2 C dt$ |
| Net propulsive efficiency | η_i | $P_{out,i} / P_{in,i} = \bar{C}_T / \bar{C}_P$ |
| Fluid vorticity | ω^* | $\nabla \times \mathbf{u}$ |
| Fluid pressure | P^* | $p / \rho u_\infty$ |

240 same mesh refinement and time step setting that has been verified for mesh independence. Each
241 numerical simulation was run for 20 cycles of undulation.

242 C. Symbolic regression method

243 The open-source symbolic regression library, PySR (Cranmer, 2023), is utilised to automat-
244 ically extract the interpretable symbolic models for net thrust force, i.e. Eq. (3), from the data
245 accumulated from the 550 simulated cases. It is based on multi-population evolutionary algorithm
246 with a special evolve-simplify-optimize cycle, being capable to high efficiency parallel compu-
247 tation with integration to deep learning tools. PySR has been proven useful in many studies,
248 including cloud cover formation (Grundner *et al.*, 2023), electron transfer rules (Li *et al.*, 2023)
249 and discovering astrophysical relations (Matchev, Matcheva, and Roman, 2022). The present study
250 chose PySR for the customisable configuration that is capable of reducing the regression time, and
251 for the parallelisation that speeds up the data-discovery speed.

252 III. RESULTS AND DISCUSSION

253 In this section, we present and discuss our discoveries from 550 cases regarding two side-
 254 by-side and anti-phase wavy NACA0012 hydrofoils in the parametric space of Reynolds number
 255 $Re = 1000 - 2000$, Strouhal number $St = 0.2 - 0.7$, and wavelength $\lambda = 0.5 - 2$. Section III A
 256 discusses how St , λ and Re influence the net thrust $\bar{C}_{T,\text{pair}}$ for each swimmer by drawing heat maps
 257 while generating a formula for a high-level summary. We also compare the simulated schooling
 258 thrust with the analytical formula describing thrust by a single swimmer (Chao, Alam, and Cheng,
 259 2022) finding interesting results. Section III B presents the dependence of net propulsive efficiency
 260 on St , λ and Re , with extra focus on the cases with the highest efficiency. In Section III C, we
 261 classify observed flow structures into several types, while connecting them to high-thrust or high-
 262 efficiency regimes.

263 A. How St , λ and Re affect net thrust $\bar{C}_{T,\text{pair}}$

264 This subsection discusses how net propulsive efficiency varies with Reynolds number $Re =$
 265 $1000 - 2000$, Strouhal number $St = 0.2 - 0.7$, and wavelength $\lambda = 0.5 - 2$. The thrust gener-
 266 ally increases with Strouhal number and wavelength, whereas the effect of Reynolds number is
 267 marginal, as demonstrated in Fig. 3. The contour line of $\bar{C}_{T,\text{pair}} = 0$ at the white region denotes the
 268 steady swimming state, which is often discussed in numerical (Borazjani and Sotiropoulos, 2008)
 269 and experimental (Li *et al.*, 2020) studies of fish swimming. With a higher St or λ , the thrust
 270 becomes positive $\bar{C}_{T,\text{pair}} > 0$, i.e. the hydrofoil school is accelerating. Conversely, with a lower St
 271 or λ , the foils are decelerating with negative thrust. Re only slightly affects this overall trend. This
 272 pattern corresponds well with the single swimmer scenario discussed in (Chao, Alam, and Cheng,
 273 2022), where the effect of Re on net thrust becomes insignificant at $Re > 1000$ while a positive
 274 correlation exists between net thrust and wavelength/Strouhal number. Here, the representative
 275 net thrust is calculated as the average value for the two swimmers, i.e. $\bar{C}_{T,\text{pair}} = (\bar{C}_{T,1} + \bar{C}_{T,2})/2$,
 276 where $\bar{C}_{T,\text{pair}} = \bar{C}_{T,1} = \bar{C}_{T,2}$ establishes for the symmetrical cases. $\bar{C}_{T,i}$ denotes the net thrust on
 277 the i th swimmer.

278 Here, we offer a high-level summary of the mean net thrust $\bar{C}_{T,\text{pair}}$ of the side-by-side and
 279 anti-phase scenarios. Following the formal analysis of previous studies regarding a flapping foil
 280 (Floryan *et al.*, 2017; Van Buren *et al.*, 2017; Alam and Muhammad, 2020) and an undulat-

ing foil (Chao, Alam, and Cheng, 2022), we use the symbolic regression tool PySR (Cranmer, 2020; Cranmer *et al.*, 2020) to automatically produce an interpretable equation that summarises the $\bar{C}_{T,\text{pair}}$ data in the present study for schooling swimmers, as seen in Eq. (3):

$$\bar{C}_{T,\text{pair}} = Re^{0.17} St^{2.03} \lambda^{1.23} - 0.26 Re^{0.19} St^{1.00} \lambda^{0.10} - 6.13 Re^{-0.6} \quad (3)$$

The summarising capability of Eq. (3) can be demonstrated in Fig. 3f, with coefficient of determination reaching $R^2 = 0.953$. For the convenience of the readers' comparison, here we also copy the $\bar{C}_{T,\text{pair}}$ equation by (Chao, Alam, and Cheng, 2022) for a single swimmer as:

$$\bar{C}_{T,\text{single}} = 0.36 Re^{0.208} St^3 \lambda - 6.13 Re^{-0.6} \quad (4)$$

We can see that compared with the single swimmer thrust $\bar{C}_{T,\text{single}}$ formula produced by Chao, Alam, and Cheng (2022), the additional mirror-symmetric swimmer casts an interesting effect on the $\bar{C}_{T,\text{pair}}$ of each schooling member. Wavelength is almost linearly correlated with net thrust as $\bar{C}_{T,\text{pair}} \sim \lambda^{1.23}$ when the Strouhal number and wavelength are relatively small, with the scaling exponent being slightly larger than $\bar{C}_{T,\text{pair}} \sim \lambda^{1.00}$. So the wavelength is slightly more influential to the thrust during schooling compared with the single swimming condition. On the other hand, the primary scaling of thrust coefficient with Strouhal number is reduced from $\bar{C}_{T,\text{single}} \sim St^3$ for a single foil (Chao, Alam, and Cheng, 2022) to $\bar{C}_{T,\text{pair}} \sim St^2$ in Eq. (3) with an additional negative term as $-0.26 Re^{0.19} St^{1.00} \lambda^{0.10}$, so the contribution from Strouhal number to net thrust becomes less significant for the present schooling scenario compared with the single swimmer case. In contrast, the scaling exponent of 2.03 in Eq. (3) is very close to that of two side-by-side pitching foils, which scale as $\bar{C}_{T,\text{pair}} \sim St^2$ (Gungor and Hemmati, 2021). In Eq. (3), the third term $-6.13 Re^{-0.6}$ indicates that, for stationary hydrofoils, i.e. $St = 0$, the unseparated boundary layer causes the domination of fluid drag force (Chao, Alam, and Cheng, 2022). $\bar{C}_{T,\text{pair}}$ increases slowly with Re due to reduced viscous force. As Re grows, the third term diminishes towards zero.

Despite minor scaling for St , side-by-side schooling can lead to significant net thrust amplification $\bar{C}_{T,\text{pair}}/\bar{C}_{T,\text{single}}$ compared with single swimming condition, as seen in Fig. 4. Generally speaking, at higher wavelength $\lambda > 0.4$ and Strouhal number $St > 0.7$, the net thrust/acceleration from schooling can be higher than a single wavy foil. Furthermore, at $\lambda > 1.1$ and $0.4 < St < 0.45$, the net thrust for each schooling swimmer can be more than ten times larger than a single swimmer! A lower Reynolds number amplifies the schooling advantage for thrust. This advantageous range of St and λ also corresponds well with the natural *carangiform* fish species with $St \approx 0.4$ (Borazjani

This is the author's peer reviewed, accepted manuscript. However, the online version of record will be different from this version once it has been copyedited and typeset.

PLEASE CITE THIS ARTICLE AS DOI: 10.1063/5.0155661

Accepted to Phys. Fluids 10.1063/5.0155661

311 and Sotiropoulos, 2008). So a better thrust performance can be another reason to school together
 312 in addition to energy conservation (Daghooghi and Borazjani, 2015; Li *et al.*, 2020). This obser-
 313 vation might be able to explain why fish school together from the perspective of net thrust; such
 314 acceleration can be significant for the predator-prey interaction (Triantafyllou, Weymouth, and
 315 Miao, 2016), thus being correlated to the survivorship of swimmers. The maximum amplification
 316 factor is obtained at $Re = 1000$ reaching $\bar{C}_{T,pair}/\bar{C}_{T,single} = 13$ at $St = 0.3$ and $\lambda = 2$, as illustrated
 317 in Fig. 4a. Maximum amplification factor $\bar{C}_{T,pair}/\bar{C}_{T,single}$ generally drops with Reynolds number,
 318 as demonstrated in Fig. 4f. This result indicates that a higher wavelength $\lambda = 2$ is advantageous
 319 for a single swimmer accelerating from low speed/Reynolds number (Du Clos *et al.*, 2019) and
 320 even more beneficial for each schooling swimmer. In addition, we should note that schooling can
 321 be less advantageous than swimming alone at $\bar{C}_{T,pair}/\bar{C}_{T,single} < 1$, located at $0.5 < \lambda < 0.7$ and
 322 $St > 0.45$, although in the present parametric space, schooling can yield much better performance
 323 in most cases.

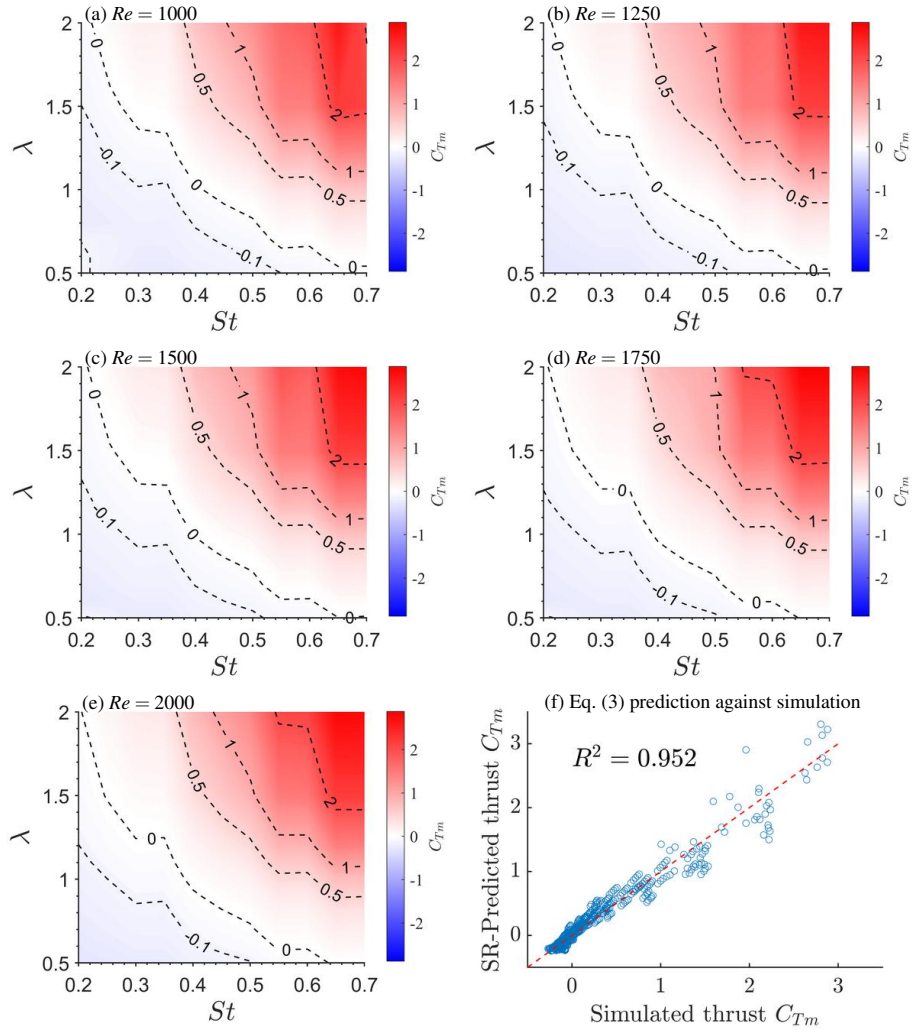


Figure 3. Heat map for mean net thrust $\bar{C}_{T, \text{pair}}$ at Strouhal number $St = 0.2 - 0.7$, wavelength $\lambda = 0.5 - 2$ and Reynolds numbers at (a) $Re = 1000$ (b) $Re = 1250$ (c) $Re = 1500$ (d) $Re = 1750$ (e) $Re = 2000$. (f) Symbolic regression prediction accuracy comparing simulation results and Eq. (3). The thrust on two swimmers is identical due to the symmetrical situation. The positive thrust, i.e. forward acceleration, is indicated by the positive values with red colour. Conversely, the negative thrust, i.e. deceleration, is indicated by the negative values with blue colour. The contour line of $\bar{C}_{T, \text{pair}} = 0$ represents the zero net thrust scenarios, i.e. steady swimming state. Only marginal differences can be observed across various Reynolds numbers.

This is the author's peer reviewed, accepted manuscript. However, the online version of record will be different from this version once it has been copyedited and typeset.

PLEASE CITE THIS ARTICLE AS DOI: 10.1063/5.0155661

Accepted to Phys. Fluids 10.1063/5.0155661

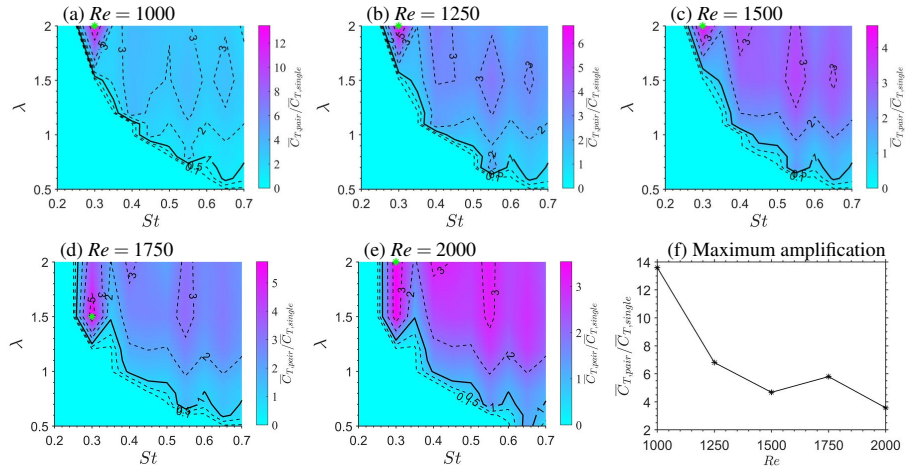


Figure 4. Heat map for schooling thrust amplification factor $\bar{C}_{T,pair}/\bar{C}_{T,single}$ at Strouhal number $St = 0.2 - 0.7$, wavelength $\lambda = 0.5 - 2$ and Reynolds numbers at (a) $Re = 1000$ (b) $Re = 1250$ (c) $Re = 1500$ (d) $Re = 1750$ (e) $Re = 2000$ (f) Maximum thrust amplification due to schooling. Here, we only show the results with both $\bar{C}_{T,pair} > 0$ and $\bar{C}_{T,single} > 0$; other non-accelerating cases are drawn as zero. This map demonstrates how schooling contributes to the thrust/acceleration of the swimmers. The thick contour line of $\bar{C}_{T,pair}/\bar{C}_{T,single} = 1$ indicates that thrust from schooling equals that from a single foil. $\bar{C}_{T,pair}/\bar{C}_{T,single} > 1$ means that each schooling member produces higher thrust than a single swimmer, and vice versa for $\bar{C}_{T,pair}/\bar{C}_{T,single} < 1$. The green marker denotes the location for the highest thrust amplification for each Reynolds number. At high St and λ , schooling can produce more thrust. Further, the schooling thrust can be several times higher than a single swimmer, especially at $St = 0.3 - 0.35$ and $\lambda \leq 1.5$. A lower Reynolds number amplifies the schooling advantage for thrust. This advantageous range of St and λ also corresponds well with a single *carangiform* fish at $St \approx 0.4$ (Borazjani and Sotiropoulos, 2008) and other swimming and flying animals at $0.2 < St < 0.4$ (Taylor, Nudds, and Thomas, 2003; Triantafyllou, Triantafyllou, and Gopalkrishnan, 1991). So a better thrust performance can be another reason to school together in addition to energy conservation (Daghooghi and Borazjani, 2015; Li *et al.*, 2020).

324 B. Dependence of net propulsive efficiency on St , λ and Re

325 The present paper defines net propulsive efficiency as $\eta_i = \bar{C}_{T, \text{pair}} / \bar{C}_p$. We note that this formula
 326 measures how efficiently the input power is converted to the net thrust, i.e. acceleration (Maertens,
 327 Triantafyllou, and Yue, 2015), as the present study is meant to focus on the problem of accelera-
 328 tion. More discussion and review of the recent development in the efficiency metrics can be found
 329 in the appendix from Lin *et al.* (2023). Since the two swimmers are placed side-by-side in anti-
 330 phase, the deforming solid is mirror-symmetric in time and space. Therefore, the resulting flow
 331 pattern is symmetrical for most cases in the present study (discussed later in detail). As a result,
 332 the thrust for each schooling member can be equivalent to each other $\eta_1 = \eta_2$ in most cases. So
 333 in the present study, net propulsive efficiency is represented by averaging the values from each of
 334 the two schooling swimmers $\eta = (\eta_1 + \eta_2)/2$.

335 Net propulsive efficiency η is generally higher in the range of $St > 0.4$ and $0.8 < \lambda < 1.5$, as
 336 seen in Fig. 5. The highest efficiency is obtained at $\lambda = 1.1, 1.2$ with $St = 0.50, 0.55$. The optimal
 337 Strouhal number $St = 0.5$ matches the observed value for a single linear-accelerating fish, e.g.
 338 Crevalle jack (Akanyeti *et al.*, 2017), but slightly higher than that for most steady-swimming fish
 339 in nature (Borazjani and Sotiropoulos, 2008). The maximum efficiency and high-efficiency region
 340 $\eta > 24\%$ both increase with Reynolds number. The highest efficiency increases almost linearly
 341 with the Reynolds number, which indicates that thrust generation can be less energy-consuming
 342 at a higher swimming/flow speed. The high-efficiency band is approximately located on the line
 343 $\lambda + 3St = 2.9$, which means that to achieve high efficiency, swimmers cannot choose both high
 344 wavelength $\lambda > 1.5$ and high Strouhal number $St > 5.5$ at the same time.

345 Net propulsive efficiency for mirror-symmetric schooling η_{pair} can be much higher than that of
 346 single swimming η_{single} , reaching $\eta_{\text{pair}}/\eta_{\text{single}} = 5$, as seen in Fig. 6. The thick line indicates the
 347 locations where $\eta_{\text{pair}}/\eta_{\text{single}} = 1$, i.e. schooling and single swimming yields identical propelling
 348 efficiency. It is seen that schooling can be more efficient at $0.25 < St < 0.55$ and $\lambda > 1$. The
 349 schooling efficiency can be several times higher than a single swimmer, especially at $St = 0.3 -$
 350 0.35 and $\lambda \leq 1.5$. A lower Reynolds number amplifies the schooling advantage for efficiency.
 351 In short, mirror-symmetric schooling can be more advantageous at low Reynolds numbers and
 352 Strouhal numbers, but higher wave lengths.

353 In addition, for clarification, given *steady swimming* condition, the Strouhal number of fish
 354 swimming ranges from 0.25 to 0.4 (Borazjani and Sotiropoulos, 2008). However, in the present

This is the author's peer reviewed, accepted manuscript. However, the online version of record will be different from this version once it has been copyedited and typeset.

PLEASE CITE THIS ARTICLE AS DOI: 10.1063/5.0155661

Accepted to Phys. Fluids 10.1063/5.0155661

study, we focus on the fish swimming with *linear acceleration* condition, which can be slightly different. The optimal Strouhal number for efficient force production can reach $St \approx 0.5$ for certain fish species (Akanyeti *et al.*, 2017). For example, Crevalle jack, Indo-Pacific tarpon, and Mangrove snapper achieve optimal propulsive efficiency at $St = 0.51, 0.48, 0.48$, which means that the optimal Strouhal number of 0.5 concluded in the present study actually matches the biological observations for at least some fish species.

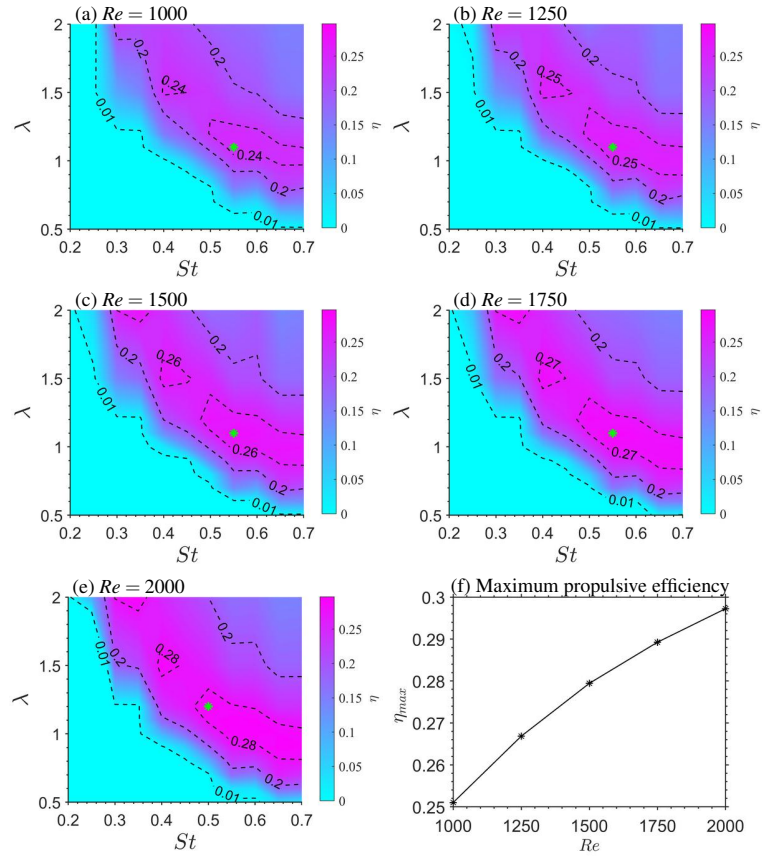


Figure 5. Heat map for net propulsive efficiency η at Strouhal number $St = 0.2 - 0.7$, wavelength $\lambda = 0.5 - 2$ and Reynolds numbers at (a) $Re = 1000$ (b) $Re = 1250$ (c) $Re = 1500$ (d) $Re = 1750$ (e) $Re = 2000$. (f) Maximum net propulsive efficiency η_{\max} at each Reynolds number. Due to spatial symmetry at any instant, net propulsive efficiency is identical for each swimmer or two swimmers as a group. The highest efficiency is denoted by the green star marker, located at $(St, \lambda) = (0.55, 1.1)$ for $Re = 1000 - 1750$ and $(St, \lambda) = (0.5, 1.2)$ for $Re = 2000$. The optimal Strouhal number $St = 0.5$ matches the observed value for a single linear-accelerating fish, e.g. Crevalle jack (Akanyeti *et al.*, 2017), but slightly higher than that for most steady-swimming fish in nature (Borazjani and Sotiropoulos, 2008). The maximum efficiency and high-efficiency region $\eta > 24\%$ both increase with Reynolds number. The cases with negative thrust are drawn as zero. The maximum efficiency increases almost linearly with Reynolds number.

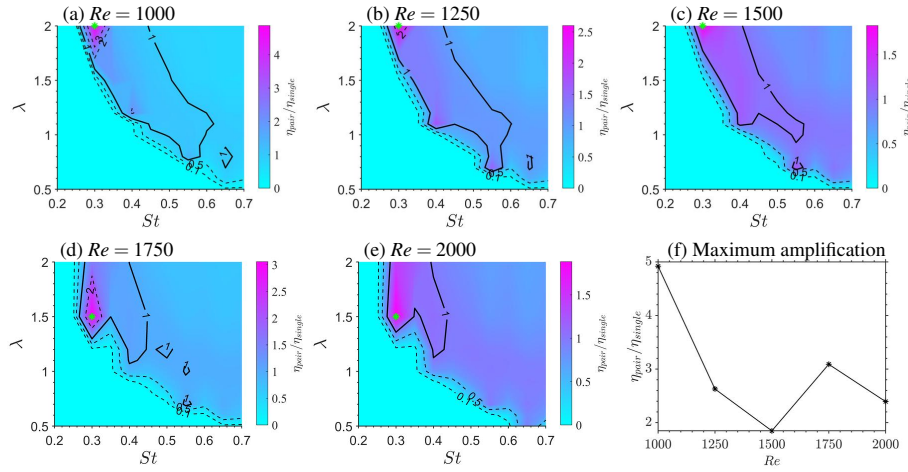


Figure 6. Heat map for schooling efficiency amplification factor $\eta_{\text{pair}}/\eta_{\text{single}}$ at Strouhal number $St = 0.2 - 0.7$, wavelength $\lambda = 0.5 - 2$ and Reynolds numbers at (a) $Re = 1000$ (b) $Re = 1250$ (c) $Re = 1500$ (d) $Re = 1750$ (e) $Re = 2000$ (f) Maximum efficiency amplification at each Re due to schooling. Here, we only show the results with both $\bar{C}_{T,\text{pair}} > 0$ and $\bar{C}_{T,\text{single}} > 0$, and the non-accelerating cases are drawn as zero. This map demonstrates how schooling contributes to the propulsive efficiency of the swimmers. The thick contour line of $\eta_{\text{pair}}/\eta_{\text{single}} = 1$ indicates equivalent propulsive efficiency from schooling and of a single foil. $\eta_{\text{pair}}/\eta_{\text{single}} > 1$ means that schooling swimmers produces higher propulsive efficiency than a single swimmer, and vice versa for $\eta_{\text{pair}}/\eta_{\text{single}} < 1$. The green marker denotes the location for the highest efficiency amplification for each Reynolds number. The schooling efficiency can be several times higher than a single swimmer, especially at $St = 0.3 - 0.35$ and $\lambda \leq 1.5$. A lower Reynolds number amplifies the schooling advantage for efficiency.

361 C. Flow structures maps

362 Here, we classify the flow structures of various scenarios based on the overall characteristics,
363 vortex shedding, and flow symmetry. In the parametric space of the present study, we can classify
364 the flow structures into six types: (a) steady wake, (b) quasi-Karman wake, (c) 2S, (d) 2P-diverge,
365 (e) 2P-converge, and (f) symmetry breaking, as demonstrated in Fig. 7. The first five types are
366 mirror-symmetric in time and space, whereas the sixth type demonstrates a chaotic flow structure
367 with symmetry breaking. Here, we explain the main characteristics of each type:

- 368 (a) Steady wake: steady streaming in the far field without vortex formation
- 369 (b) Quasi-Karman wake: intermediate state between steady streaming and Karman vortex shed-
370 ding
- 371 (c) 2S: a single vortex shed from each wavy foil per cycle, forming a vortex dipole with the
372 main streaming direction pointing downstream
- 373 (d) 2P-diverge: one vortex dipole per cycle per foil, forming two reverse vortex streets towards
374 diverging directions
- 375 (e) 2P-converge: similar to 2P-diverge, yet the vortex dipoles are converging instead of diverg-
376 ing
- 377 (f) Symmetry breaking: Symmetrical wake breaks, resulting asymmetric flow pattern

378 This intensity of vorticity and irregularity both increases with the order listed above. For example,
379 the steady wake (a) contains the lowest overall vorticity intensity with stable flow structures, and
380 vice versa for the symmetry breaking (f) case.

381 Based on this classification, we generate a set of maps to illustrate the distribution of flow
382 structures in the present parametric space, as shown in Fig. 7; the detailed demonstration for all
383 cases can be found in Appendix A. The markers correspond to the types listed in Fig. 7. In general,
384 the variation of $Re = 1000 - 2000$ is not significantly affecting the flow structure distribution; so
385 we mainly discuss the effects of λ and St . The steady wake (a) is only observed at very low
386 wavelength $\lambda \leq 0.6$ and Strouhal number $St \leq 0.3$, where the flow is not heavily disturbed. The
387 quasi-Karman wake (b) is observed at slightly higher λ and St , and even higher for the 2S (c) cases.
388 The conversion from quasi-Karman wake (b) to 2S (c) occurs at approximately $4.67St + \lambda = 2.367$.

389 2P-diverge (d) accounts for the most number of cases in the present study. The transition from
390 2S (c) to 2P-diverge (d) is observed at approximately $4.5St + \lambda = 2.85$. 2P-converge (e) can
391 be identified at roughly $2.67St + \lambda = 3.067$. The 2P-converge is a boundary condition between
392 the 2P-diverge (d) and the full development of symmetry breaking (f), so only a few cases can
393 be discovered. Furthermore, at $2.67St + \lambda > 3.067$, the flow becomes asymmetric and highly
394 irregular.

395 The region of high net thrust from Fig. 3 corresponds to the symmetry breaking (f) region in
396 Fig. 8. Zero net thrust cases, i.e. steady-swimming, partly overlap with the boundary between
397 2S (c) and 2P-diverge (d). So the positive net thrust, i.e. acceleration, mainly corresponds with
398 flow structures of 2P-diverge (d), 2P-converge (e) and symmetry breaking (f). High thrust is
399 found in the symmetry breaking (f) condition, so the irregular flow pattern does not significantly
400 affect the thrust generation. The region of high net propulsive efficiency from Fig. 5 overlaps
401 with the distribution of the 2P-diverge (d) pattern in Fig. 8. Cases with the highest efficiency all
402 demonstrate 2P-diverge (d) pattern. Therefore, the structural vortex dipole shedding contributes
403 to higher efficiency. Conversely, the symmetry breaking (f) region cannot yield high efficiency.
404 While comparing schooling thrust amplification in Fig. 4 and the flow structure map of Fig. 8, it
405 is interesting to note that the most significant schooling amplification factor $\bar{C}_{T,pair}/\bar{C}_{T,single}$ is all
406 located in the 2P-converge (e) region, which corresponds to the s-RKV region of a single swimmer
407 (Chao, Alam, and Cheng, 2022), featuring a skewed reverse Karman vortex street. This indicates
408 that schooling members can produce more thrust from two converging skewed vortex streets.

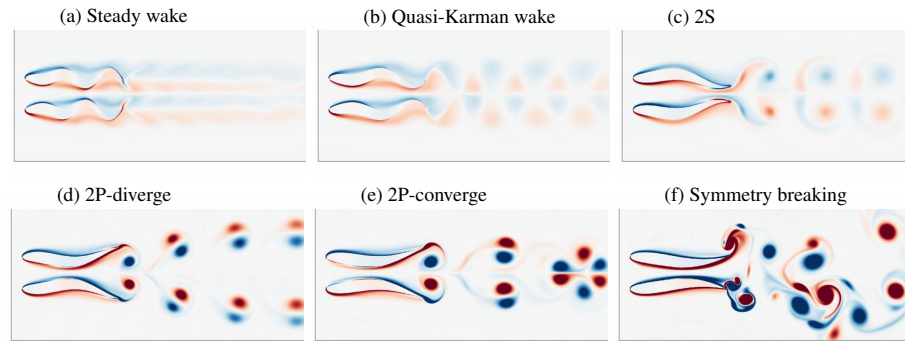


Figure 7. Representative examples for six flow structures identified as: (a) steady wake: steady streaming in the far field wake (b) quasi-Karman wake: periodically disturbed wake but no distinct vortex (c) 2S: one vortex from each foil (d) 2P-diverge: a pair of vortices *diverging* in the wake (e) 2P-converge: a pair of vortices *converging* in the wake (f) Symmetry breaking: an unstable flow that is asymmetric Here, the red colour denotes positive vorticity (counter-clockwise) with the blue colour representing the negative vorticity (clockwise).

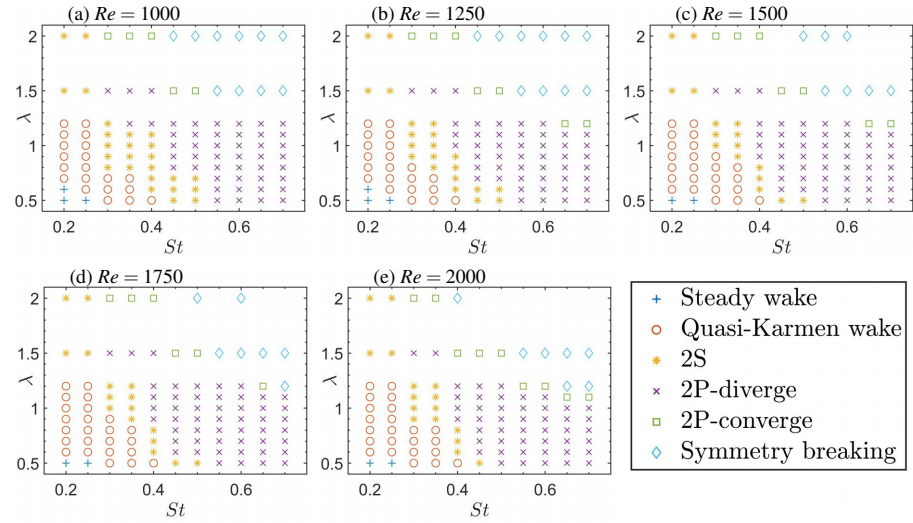


Figure 8. Flow structure classification at Strouhal number $St = 0.2 - 0.7$, wavelength $\lambda = 0.5 - 2$ and Reynolds numbers at (a) $Re = 1000$ (b) $Re = 1250$ (c) $Re = 1500$ (d) $Re = 1750$ (e) $Re = 2000$. The alphabetic marker types correspond to the classification shown in Fig. 7.

409 D. Investigation of Fluid Mechanism

410 The Reynolds number, wavelength, and Strouhal number show substantial variations that ultimately result in a distinct difference in the flow structure and corresponding underlying mechanisms. Concurrent with the variation in flow structure, significant changes in performance metrics, 412 *i.e.*, thrust and efficiency, are observed. In this section, to delve deeper into the mechanisms, three 413 typical cases are selected for a detailed analysis and comparative study. The cases are analysed 414 using fluid vorticity, net force, pressure distribution, and fluid velocity vectors. 415

416 The selected cases for our investigation are presented in Table 3. Each case represents a consistent increment in input values: the Reynolds number increases by 500, the Strouhal number 417 by 0.1, and the wavelength by 0.3. These cases are chosen to represent different flow structures, 418 namely: 2S in the first case, 2P-diverge in the second case, and symmetry breaking in the third 419 case. To facilitate comparison, we maintain identical colour scales for vorticity, pressure, and 420 velocity vectors across these cases. 421

Table 3. Representative cases for in-depth study and comparison

| No. | Re | St | λ | Flow Structure | $\tilde{C}_{T,pair}$ | η_{pair} | Vorticity & Force | Pressure & Velocity |
|-----|------|------|-----------|------------------------|----------------------|---------------|-------------------|---------------------|
| 1st | 1000 | 0.4 | 0.9 | 2S (Fig. 7c) | -0.059 | N/A | Fig. 9 | Fig. 10 |
| 2nd | 1500 | 0.5 | 1.2 | 2P-diverge (Fig. 7d) | 0.403 | 27.5% | Fig. 11 | Fig. 12 |
| 3rd | 2000 | 0.6 | 1.5 | Sym-breaking (Fig. 7f) | 1.527 | 21.4% | Fig. 13 | Fig. 14 |

422 In the first case at $Re = 1000$, $St = 0.4$, and $\lambda = 0.9$, each hydrofoil sheds two vortices per un-
423 dulation cycle. The generated thrust force profiles are nearly identical between the hydrofoils, with
424 peak thrust corresponding to the shedding of stronger vortices (Fig. 9i-9j). The primary pressure
425 fluctuation occurs between the swimmers (Fig. 10), with high thrust related to high downstream
426 fluid velocity and rapid dissipation of negative pressure downstream. A two-row vortex array
427 accounts for velocity vector fluctuations in the wake.

428 The similarity in the thrust force profiles between the two swimmers (Fig. 9i-9j) is noteworthy,
429 with two peaks at instants c and g associated with maximum instantaneous thrust. Interestingly,
430 the shedding of the stronger vortex corresponds to the higher thrust peak at instant c, while the
431 formation of a smaller, short-lived vortex results in a smaller thrust peak at instant g. On the
432 contrary, the thrust trough at instant h corresponds to the complete shedding of the minor vortex,

which lacks the necessary strength to generate sufficient thrust. Significant pressure fluctuations primarily occur in the gap between the two swimmers, as illustrated in Fig. 10. The maximum positive pressure, which aligns with low thrust, is attained at the instant a in the gap, resulting in a high lift force that separates the swimmers. In contrast, at instant e, the pressure in the gap hits a negative maximum, where the thrust is close to the local minimum, and the lift turns positive, drawing the swimmers together.

Furthermore, high thrust at instant b is achieved when strong positive pressure is exerted at the posterior part of the swimmers, propelling them forward. At instant c, the swimmers are "sucked" forward due to strong negative pressure at their front. In the downstream area, the vortex shedding creates negative pressure (Fig. 10g) which dissipates rapidly within one cycle. By analysing the velocity field, we discovered that high thrust aligns with high fluid velocity towards the downstream direction, "propelling" the swimmers forward. The two-row vortex array in the wake introduces velocity vector fluctuations that follow a similar pattern.

In the second case, with $Re = 1500$, $St = 0.5$, and $\lambda = 1.2$, we identify a distinctive "2P-diverge" flow pattern in the wake of the two swimmers, wherein the outer vortex exhibits greater persistence and influences the vortex direction alignment. Instances of simultaneous high pressures at the ends of the swimmers produce high net thrust.

Observation of the vorticity distribution (Fig. 11) reveals that two distinct rows of vortex dipoles are propelled from the swimmers' posterior part, forming the unique "2P-diverge" flow structure pattern, contrasting markedly with the "2S" pattern of the first case. The vortex shedding mechanism is similar to the first case, with each undulation cycle of the hydrofoils generating two vortices. However, the outer vortex persists rather than dissipating, resulting in vortex dipoles propelled away from the mirror-symmetric axis between the swimmers. The outer vortex's rapid dissipation compared to the inner one can be ascertained from the vorticity and pressure distribution (Fig. 11 and 12). As the dissipation progresses, the vortex dipoles' moving direction gradually aligns with the free-stream velocity. Mirroring the first case, the time history of the thrust force features two peaks and one trough. The major and minor peaks are located at instant d and h, respectively. It is intriguing that these instants of high net thrust coincide with high positive and negative pressure at the swimmers' posterior and anterior parts, respectively (Fig. 12). This observation suggests that the swimmer is simultaneously "pushed" and "pulled" by the positive and negative pressure at different locations, contributing to high instantaneous thrust. The larger peak at instant d occurs when positive pressure is on the outside, and negative pressure is in the gap. The

465 thrust at instant h is weaker due to the formation of the vortex pair near the tails, which slightly
466 reduces the pressure in the gap.

467 In the third case, at $Re = 2000$, $St = 0.6$, and $\lambda = 1.5$, despite irregular wake flow and symmetry
468 breaking, the fluid-structure interaction mechanism aligns largely with the second case exhibiting
469 the 2P-diverge pattern. The near-tail flow field maintains substantial regularity and symmetry.

470 In the third case, as depicted in Fig. 13 and 14, the flow structure exhibits irregularity with
471 symmetry breaking, although the vortices near the tails remain largely regular and symmetric.
472 Like to the second case, each hydrofoil generates a pair of vortices in a complete cycle. The
473 vortex dipoles shed from each foil rapidly converge whilst interacting with previously generated
474 vortices, leading to irregularity in the flow field. This pattern differs from the second case, where
475 the vortex sheddings symmetrically diverge rather than quickly impinge on each other. Despite the
476 irregular wake flow, the net thrust and lift force time history between the two swimmers remain
477 strikingly identical, as seen in Fig. 13i and 13j. Furthermore, the correlation between pressure
478 distribution and force variation strongly resembles to the second case with the 2P-diverge pattern.
479 High thrust is observed when the swimmers are "pushed" and "pulled" by the positive and negative
480 pressure at the posterior and anterior parts of the hydrofoil body. However, the vortex pair in the
481 gap slightly mitigates the thrust at instant g, as seen in Fig. 14g. Regarding the wake region, here,
482 the pressure disturbance is significantly more pronounced compared with the previous cases, due
483 to the strong negative pressure created by the recirculation and interaction of the vortices.

This is the author's peer reviewed, accepted manuscript. However, the online version of record will be different from this version once it has been copyedited and typeset.

PLEASE CITE THIS ARTICLE AS DOI: 10.1063/5.0155661

Accepted to Phys. Fluids 10.1063/5.0155661

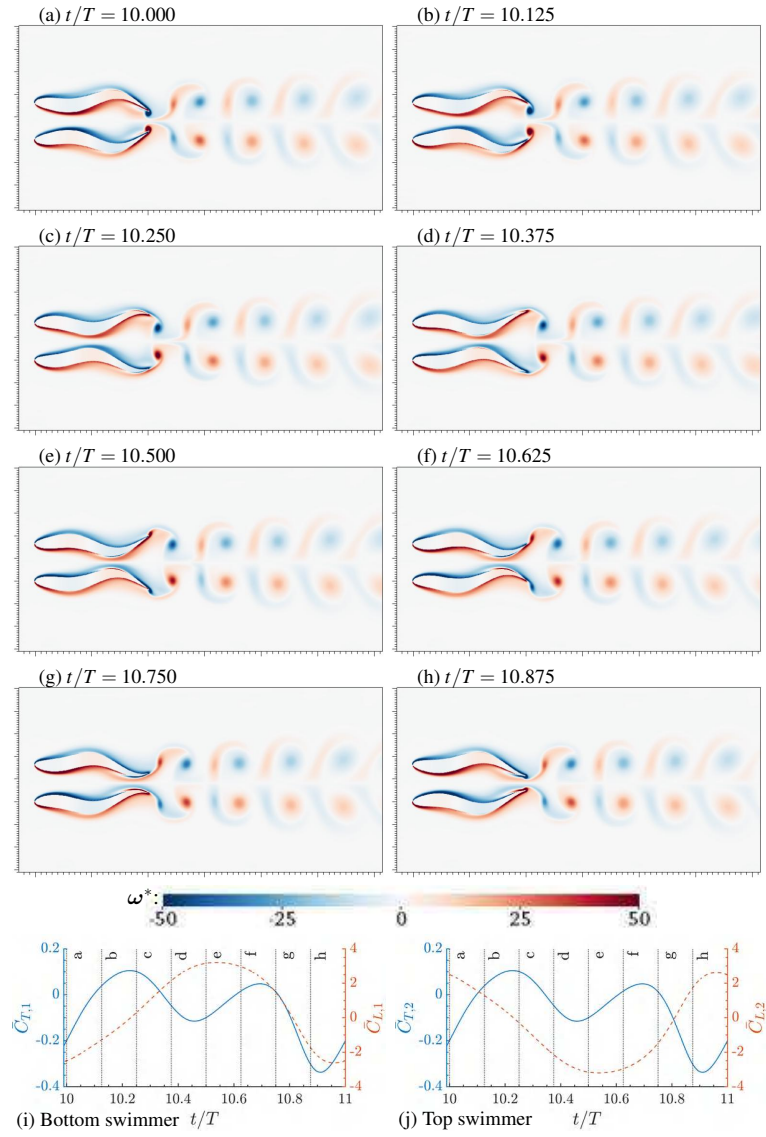


Figure 9. Vorticity contours and hydrofoil deformation with $Re = 1000$, $St = 0.4$, $\lambda = 0.9$, at instants of a typical period (a-h) $t/T = 10.000 - 10.875$. Time histories of thrust and lift coefficient for the (i) Bottom and (j) Top swimmers.

This is the author's peer reviewed, accepted manuscript. However, the online version of record will be different from this version once it has been copyedited and typeset.

PLEASE CITE THIS ARTICLE AS DOI: 10.1063/5.0155661

Accepted to Phys. Fluids 10.1063/5.0155661

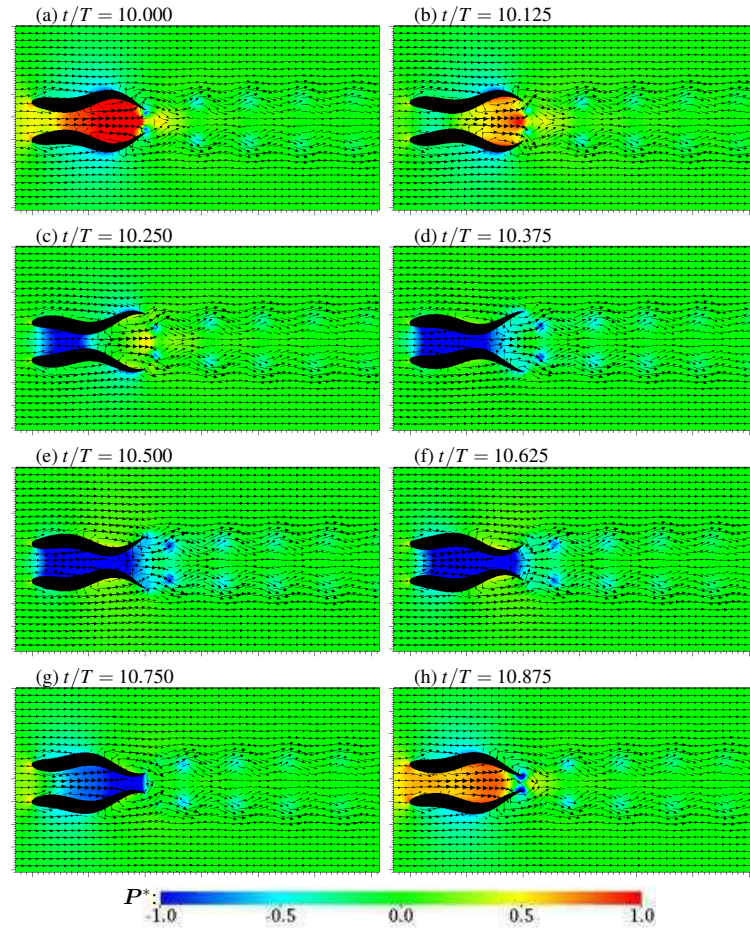


Figure 10. Pressure contours, velocity vectors and hydrofoil deformation with $Re = 1000$, $Sr = 0.4$, $\lambda = 0.9$, at instants of a typical period (a-h) $t/T = 10.00 - 10.875$. Time histories of thrust and lift coefficient for the (i) Bottom and (j) Top swimmers.

This is the author's peer reviewed, accepted manuscript. However, the online version of record will be different from this version once it has been copyedited and typeset.

PLEASE CITE THIS ARTICLE AS DOI: 10.1063/5.0155661

Accepted to Phys. Fluids 10.1063/5.0155661

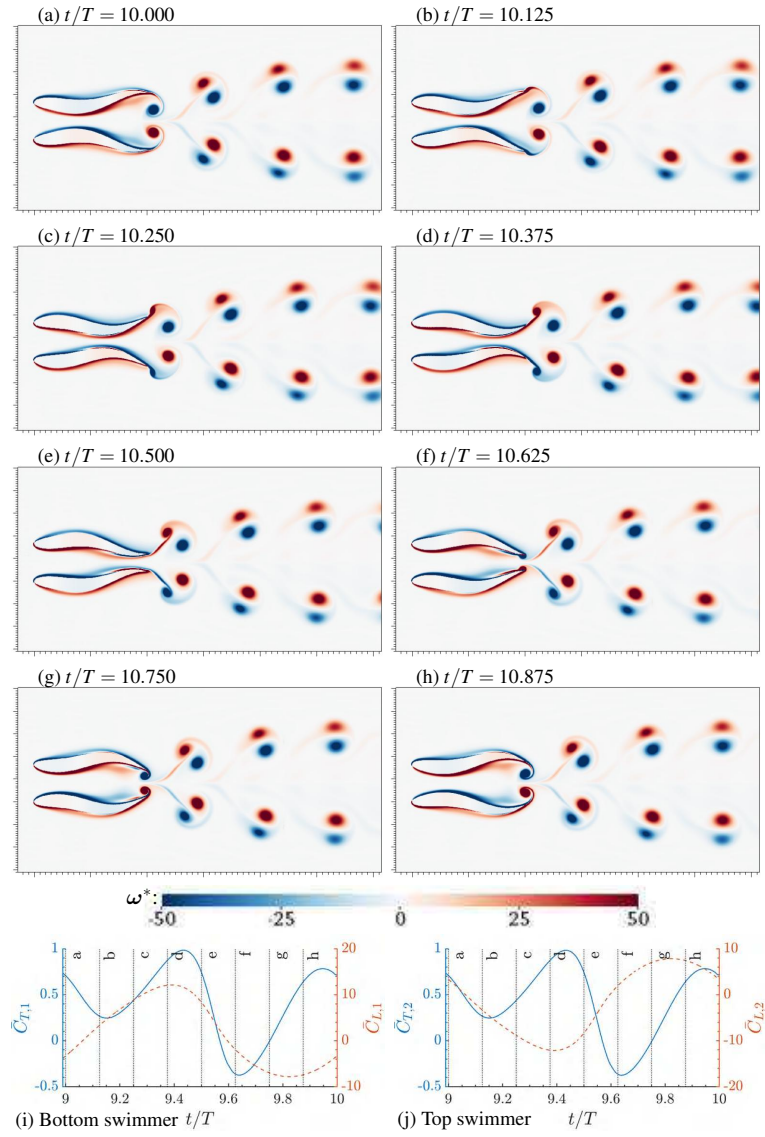


Figure 11. Vorticity contours and hydrofoil deformation with $Re = 1500$, $St = 0.5$, $\lambda = 1.2$, at instants of a typical period (a-h) $t/T = 10.00 - 10.875$. Time histories of thrust and lift coefficient for the (i) Bottom and (j) Top swimmers.

This is the author's peer reviewed, accepted manuscript. However, the online version of record will be different from this version once it has been copyedited and typeset.

PLEASE CITE THIS ARTICLE AS DOI: 10.1063/5.0155661

Accepted to Phys. Fluids 10.1063/5.0155661

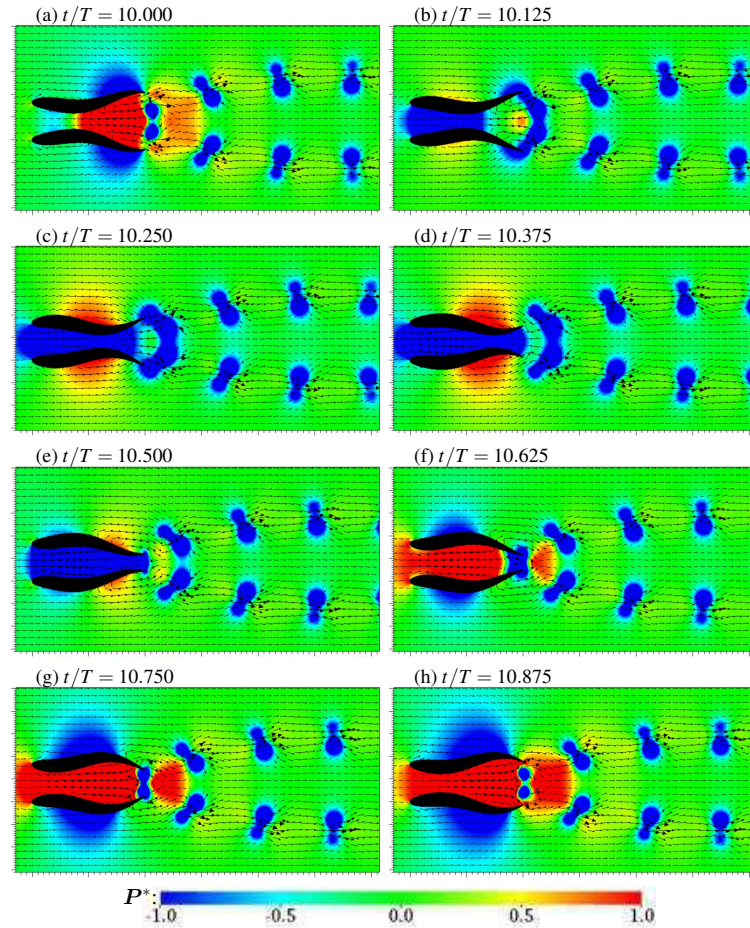


Figure 12. Pressure contours, velocity vectors and hydrofoil deformation with $Re = 1500$, $Sr = 0.5$, $\lambda = 1.2$, at instants of a typical period (a-h) $t/T = 10.00 - 10.875$. Time histories of thrust and lift coefficient for the (i) Bottom and (j) Top swimmers.

This is the author's peer reviewed, accepted manuscript. However, the online version of record will be different from this version once it has been copyedited and typeset.

PLEASE CITE THIS ARTICLE AS DOI: 10.1063/5.0155661

Accepted to Phys. Fluids 10.1063/5.0155661

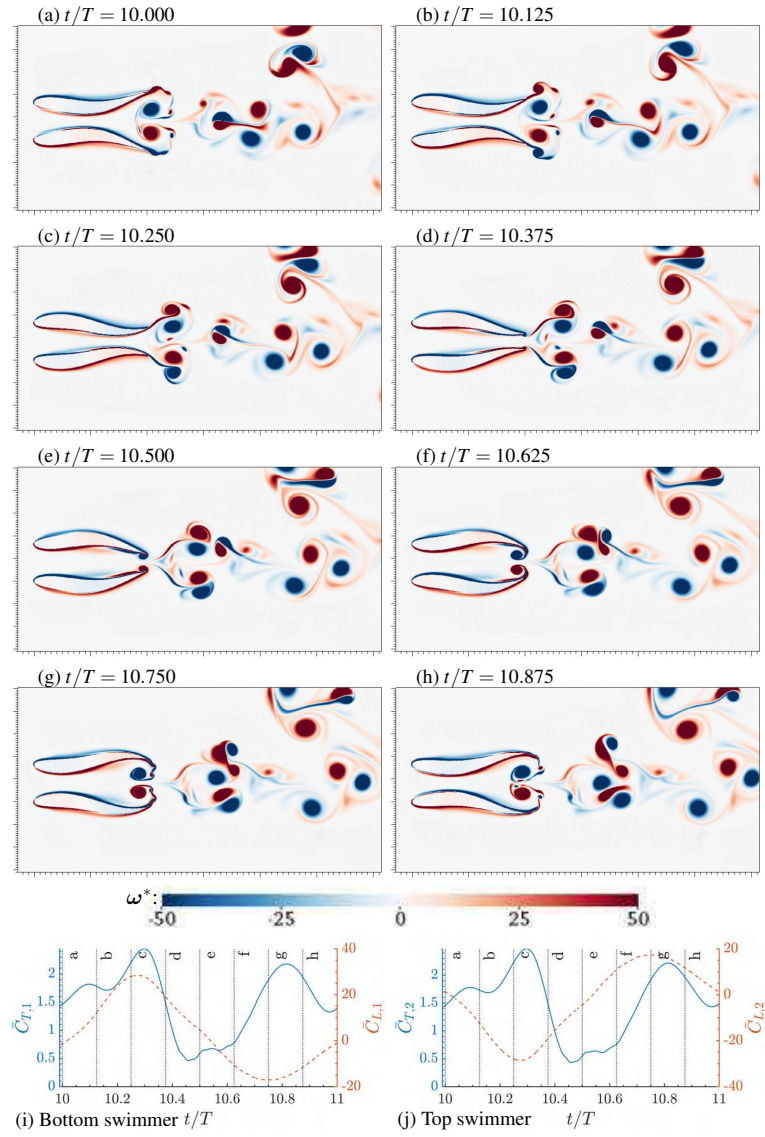


Figure 13. Vorticity contours and hydrofoil deformation with $Re = 2000$, $St = 0.6$, $\lambda = 1.5$, at instants of a typical period (a-h) $t/T = 10.00 - 10.875$. Time histories of thrust and lift coefficient for the (i) Bottom and (j) Top swimmers.

This is the author's peer reviewed, accepted manuscript. However, the online version of record will be different from this version once it has been copyedited and typeset.

PLEASE CITE THIS ARTICLE AS DOI: 10.1063/5.0155661

Accepted to Phys. Fluids 10.1063/5.0155661

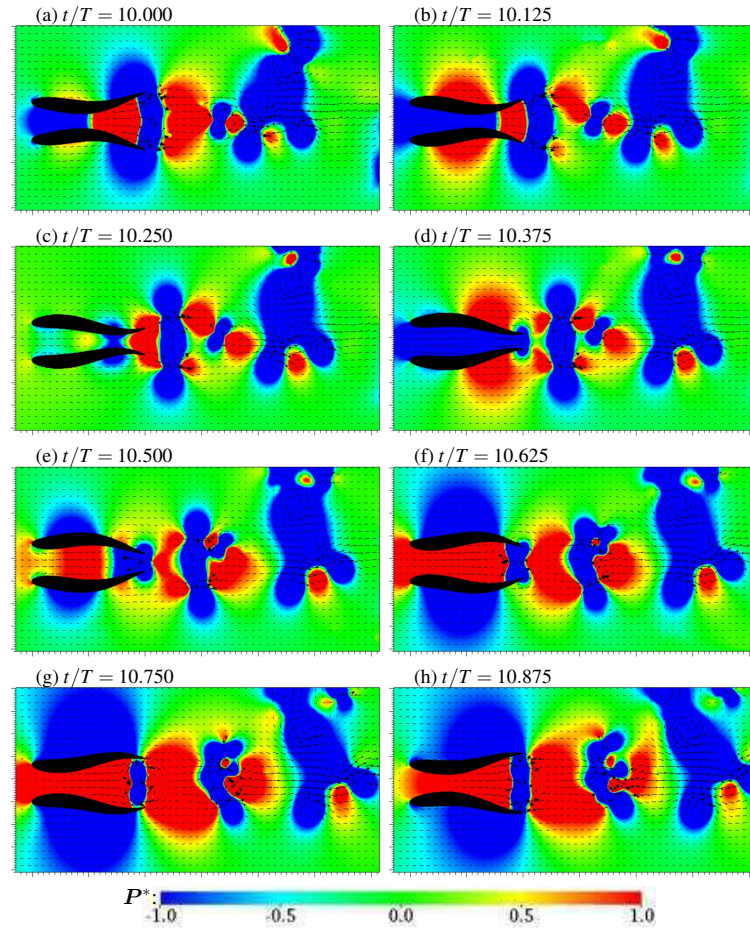


Figure 14. Pressure contours, velocity vectors and hydrofoil deformation with $Re = 2000$, $Sr = 0.6$, $\lambda = 1.5$, at instants of a typical period (a-h) $t/T = 10.00 - 10.875$. Time histories of thrust and lift coefficient for the (i) Bottom and (j) Top swimmers.

IV. CONCLUSIONS

The effects of fish body wavelength on its linear acceleration during side-by-side schooling conditions have not been studied in detail previously. In the present paper, we conducted a systematic numerical study, involving 550 cases of two linearly-accelerating side-by-side wavy NACA0012 hydrofoils swimming in anti-phase. We examined the net thrust distribution, net propulsive efficiency, and flow structures by drawing heat maps and proposing empirical formulas. The simulation is conducted on a customised version of the ConstraintIB (Bhalla *et al.*, 2013; Griffith and Patankar, 2020) module from the IBAMR (Griffith, 2013) open-source library. The parametric space is tested for Strouhal number $St = 0.2 - 0.7$, wavelength $\lambda = 0.5 - 2$ and Reynolds number $Re = 1000 - 2000$. The lateral gap distance and maximum tail amplitude are fixed at $G = 0.33$ and $A_{\max} = 0.1$, respectively. These ranges are chosen based on BCF swimmers in nature (Gazzola, Argentina, and Mahadevan, 2014; Santo *et al.*, 2021).

Here, we summarise the discoveries as follows:

1. We propose an equation as a high-level summary of the mean net thrust on each undulating swimmer: $\bar{C}_{T,\text{pair}} = Re^{0.17} St^{2.03} \lambda^{1.23} - 0.26 Re^{0.19} St^{1.00} \lambda^{0.10} - 6.13 Re^{-0.6}$.
2. Mean net thrust increases with wavelength λ and Strouhal number St , yet only slightly with Reynolds number Re in the present laminar regime. When λ and St are relatively small, the thrust increases almost linearly with wavelength $\bar{C}_{T,\text{pair}} \sim \lambda^{1.23}$ while scaling with Strouhal number as $\bar{C}_{T,\text{pair}} \sim St^2$, where the scaling-exponent being two-thirds of that for a single swimmer $\bar{C}_{T,\text{pair}} \sim St^3$ (Chao, Alam, and Cheng, 2022).
3. Side-by-side anti-phase schooling can enhance the thrust by more than ten times, as compared with a single swimmer at $\lambda \geq 1.5$ and $St = 0.3$.
4. High net propulsive efficiency η is achieved at $St > 0.4$ and $0.8 < \lambda < 1.5$, with the highest obtained at about $St = 0.5$ and $\lambda = 1.1$, which are consistent with the biological observations.
5. We classify the flow structures into six distinct types based on their flow characteristics: (a) steady wake, (b) quasi-Karman wake, (c) 2S, (d) 2P-diverge, (e) 2P-converge, (f) symmetry breaking.

512 6. Wavelength λ and Strouhal number St are more influential than Reynolds number Re in
513 determining the flow structures in the tested parametric space. The highest net thrust is
514 accompanied with symmetry breaking, whereas the high-efficiency regime corresponds to a
515 2P-diverge type wake.

516 7. Instantaneous high thrust occurs when differential pressure at the rear and front of the hy-
517 drofoil body simultaneously "pushes" and "pulls" the swimmers, respectively, while the
518 presence of a vortex pair in the intermediary space diminishes thrust when the tails move
519 outwards.

520 Based on these results, we can make a few interesting comments that help understand the
521 hydrodynamically-relevant behaviour of biological swimmers in nature or for designing a school-
522 ing strategy for biomimetic robotic underwater vehicles. Side-by-side schooling can produce much
523 higher thrust and, therefore, higher acceleration than a single BCF swimmer. This schooling ad-
524 vantage is most prominent at low Reynolds numbers, implying that the fish's swimming agility
525 improves in school. Hence, schooling may be preferred due to better survivorship associated with
526 faster acceleration. Also, in the context of schooling conditions considered here, the wavelength
527 and Strouhal number for best efficiency are $\lambda \approx 1.2$ and $St \approx 0.5$, respectively, which match the
528 observed values for a single swimmer (Borazjani and Sotiropoulos, 2008). In future, Floquet
529 analysis can be further applied to shed light on the symmetry breaking during acceleration.

530 V. LIMITATIONS AND FUTURE WORKS

531 The present study involves only 2D simulations, whereas high-fidelity 3D models can be useful
532 to real 3D flow patterns for a few cases, e.g. maximum thrust or efficiency. The present study
533 applies a tethered configuration to approximate various instants of linear acceleration, which is
534 not the most accurate and intuitive method. We will conduct more self-propelling simulations in
535 the future. Also, the conclusions regarding Reynolds number are limited to the present laminar
536 parametric space involving $Re = 1000 - 2000$. The effects of Re in transition and turbulent regimes
537 remain to be explored in the future. What is more, further analysis of the underlying mechanism
538 should require examination of added mass and added damping, etc.

539 ACKNOWLEDGMENTS

540 This work was funded by China Postdoctoral Science Foundation (Grant No. 2021M691865)
 541 and by Science and Technology Major Project of Fujian Province in China (Grant No. 2021NZ033016).
 542 We appreciate the US National Science Foundation award OAC 1931368 (A.P.S.B) for supporting
 543 the IBAMR library. This work was also financially supported by the National Natural Science
 544 Foundation of China (Grant Nos. 12074323; 42106181), the Natural Science Foundation of Fujian
 545 Province of China (No. 2022J02003), the China National Postdoctoral Program for Innovative Tal-
 546 ents (Grant No. BX2021168) and the Outstanding Postdoctoral Scholarship, State Key Laboratory
 547 of Marine Environmental Science at Xiamen University.

548 DATA AVAILABILITY STATEMENT

549 The data that support the findings of this study are available from the corresponding author
 550 upon reasonable request.

551 REFERENCES

- 552 Akanyeti, O., Putney, J., Yanagitsuru, Y. R., Lauder, G. V., Stewart, W. J., and Liao, J. C.,
 553 “Accelerating fishes increase propulsive efficiency by modulating vortex ring geometry,” Pro-
 554 ceedings of the National Academy of Sciences of the United States of America **114** (2017),
 555 10.1073/pnas.1705968115.
 556 Alam, M. M. and Muhammad, Z., “Dynamics of flow around a pitching hydrofoil,” Journal of
 557 Fluids and Structures **99** (2020), 10.1016/j.jfluidstructs.2020.103151.
 558 Ashraf, I., Bradshaw, H., Ha, T. T., Halloy, J., Godoy-Diana, R., and Thiria, B., “Simple phalanx
 559 pattern leads to energy saving in cohesive fish schooling,” Proceedings of the National Academy
 560 of Sciences of the United States of America **114** (2017), 10.1073/pnas.1706503114.
 561 Balay, S., Abhyankar, S., Adams, M. F., Brown, J., Brune, P., Buschelman, K., Dalcin, L., Ei-
 562 jkhout, V., Gropp, W. D., Kaushik, D., and Others., “PETSc web page,” (2001).
 563 Balay, S., Buschelman, K., Eijkhout, V., Gropp, W., Kaushik, D., Knepley, M., McInnes, L. C.,
 564 Smith, B., and Zhang, H., “PETSc Users Manual,” ReVision **2** (2010).

- 565 Balay, S., Gropp, W. D., McInnes, L. C., and Smith, B. F., "Efficient Management of Parallelism in
566 Object-Oriented Numerical Software Libraries," in *Modern Software Tools for Scientific Com-
567 puting* (1997).
- 568 Bhalla, A. P. S., Bale, R., Griffith, B. E., and Patankar, N. A., "A unified mathematical frame-
569 work and an adaptive numerical method for fluid-structure interaction with rigid, deforming,
570 and elastic bodies," *Journal of Computational Physics* **250** (2013), 10.1016/j.jcp.2013.04.033.
- 571 Bhalla, A. P. S., Bale, R., Griffith, B. E., and Patankar, N. A., "Fully resolved immersed electro-
572 hydrodynamics for particle motion, electrolocation, and self-propulsion," *Journal of Computa-
573 tional Physics* **256**, 88–108 (2014).
- 574 Bhalla, A. P. S., Griffith, B. E., and Patankar, N. A., "A Forced Damped Oscillation Framework
575 for Undulatory Swimming Provides New Insights into How Propulsion Arises in Active and
576 Passive Swimming," *PLoS Computational Biology* **9** (2013), 10.1371/journal.pcbi.1003097.
- 577 Bhalla, A. P. S., Nangia, N., Dafnakis, P., Bracco, G., and Mattiazzo, G., "Simulat-
578 ing water-entry/exit problems using Eulerian–Lagrangian and fully-Eulerian fictitious do-
579 main methods within the open-source IBAMR library," *Applied Ocean Research* **94** (2020),
580 10.1016/j.apor.2019.101932.
- 581 Borazjani, I., "The functional role of caudal and anal/dorsal fins during the C-start of a bluegill
582 sunfish," *Journal of Experimental Biology* **216** (2013), 10.1242/jeb.079434.
- 583 Borazjani, I. and Sotiropoulos, F., "Numerical investigation of the hydrodynamics of carangiform
584 swimming in the transitional and inertial flow regimes," *Journal of Experimental Biology* **211**
585 (2008), 10.1242/jeb.015644.
- 586 Borazjani, I. and Sotiropoulos, F., "Numerical investigation of the hydrodynamics of anguilliform
587 swimming in the transitional and inertial flow regimes," *Journal of Experimental Biology* **212**
588 (2009), 10.1242/jeb.025007.
- 589 Borazjani, I. and Sotiropoulos, F., "On the role of form and kinematics on the hydrodynamics
590 of self-propelled body/caudal fin swimming," *Journal of Experimental Biology* **213** (2010),
591 10.1242/jeb.030932.
- 592 Borazjani, I., Sotiropoulos, F., Tytell, E. D., and Lauder, G. V., "Hydrodynamics of the bluegill
593 sunfish C-start escape response: Three-dimensional simulations and comparison with experi-
594 mental data," *Journal of Experimental Biology* **215** (2012), 10.1242/jeb.063016.
- 595 Chao, L.-M., Alam, M. M., and Cheng, L., "Hydrodynamic performance of slender swimmer:
596 effect of travelling wavelength," *Journal of Fluid Mechanics* **947**, A8 (2022).

This is the author's peer reviewed, accepted manuscript. However, the online version of record will be different from this version once it has been copyedited and typeset.

PLEASE CITE THIS ARTICLE AS DOI: 10.1063/5.0155661

Accepted to Phys. Fluids 10.1063/5.0155661

- 597 Chao, L. M., Alam, M. M., and Ji, C., "Drag-thrust transition and wake structures of a pitch-
598 ing foil undergoing asymmetric oscillation," *Journal of Fluids and Structures* **103** (2021),
599 10.1016/j.jfluidstructs.2021.103289.
- 600 Chao, L. M., Pan, G., Zhang, D., and Yan, G. X., "On the two staggered swimming fish," *Chaos,*
601 *Solitons and Fractals* **123** (2019), 10.1016/j.chaos.2019.04.028.
- 602 Coombs, S. and Montgomery, J., "The role of flow and the lateral line in the multisensory guidance
603 of orienting behaviors," in *Flow Sensing in Air and Water: Behavioral, Neural and Engineering*
604 *Principles of Operation* (2014).
- 605 Cranmer, M., "PySR: Fast & Parallelized Symbolic Regression in Python/Julia," (2020).
- 606 Cranmer, M., "Interpretable Machine Learning for Science with PySR and SymbolicRegression.jl," (2023), arXiv:2305.01582 [astro-ph.IM].
- 607 Cranmer, M., Sanchez-Gonzalez, A., Battaglia, P., Xu, R., Cranmer, K., Spergel, D., and Ho,
608 S., "Discovering Symbolic Models from Deep Learning with Inductive Biases," *NeurIPS 2020*
609 (2020), arXiv:2006.11287 [cs.LG].
- 610 Daghooghi, M. and Borazjani, I., "The hydrodynamic advantages of synchronized swim-
611 ming in a rectangular pattern," *Bioinspiration and Biomimetics* **10** (2015), 10.1088/1748-
612 3190/10/5/056018.
- 613 Deng, J. and Liu, D., "Spontaneous response of a self-organized fish school to a predator," *Bioin-*
614 *spiration and Biomimetics* **16** (2021), 10.1088/1748-3190/abfd7f.
- 615 Deng, J., Shao, X. M., and Yu, Z. S., "Hydrodynamic studies on two traveling wavy foils in tandem
616 arrangement," *Physics of Fluids* **19** (2007), 10.1063/1.2814259.
- 617 Deng, J., Sun, L., Lubao Teng, Pan, D., and Shao, X., "The correlation between wake transition
618 and propulsive efficiency of a flapping foil: A numerical study," *Physics of Fluids* **28** (2016),
619 10.1063/1.4961566.
- 620 Deng, J., Teng, L., Pan, D., and Shao, X., "Inertial effects of the semi-passive flapping foil on its
621 energy extraction efficiency," *Physics of Fluids* **27** (2015), 10.1063/1.4921384.
- 622 Deng, J., Wang, S., Kandel, P., and Teng, L., "Effects of free surface on a flapping-foil based ocean
623 current energy extractor," *Renewable Energy* **181** (2022), 10.1016/j.renene.2021.09.098.
- 624 Dewey, P. A., Quinn, D. B., Boschitsch, B. M., and Smits, A. J., "Propulsive performance
625 of unsteady tandem hydrofoils in a side-by-side configuration," *Physics of Fluids* **26** (2014),
626 10.1063/1.4871024.
- 627

- 628 Domenici, P. and Hale, M. E., "Escape responses of fish: A review of the diversity in motor control,
629 kinematics and behaviour," (2019).
- 630 Dong, G. J. and Lu, X. Y., "Characteristics of flow over traveling wavy foils in a side-by-side
631 arrangement," *Physics of Fluids* **19** (2007), 10.1063/1.2736083.
- 632 Du Clos, K. T., Dabiri, J. O., Costello, J. H., Colin, S. P., Morgan, J. R., Fogerson, S. M., and
633 Gemmell, B. J., "Thrust generation during steady swimming and acceleration from rest in an-
634 guilliform swimmers," *Journal of Experimental Biology* **222** (2019), 10.1242/jeb.212464.
- 635 Eaton, R. C., Bombardieri, R. A., and Meyer, D. L., "The Mauthner-initiated startle response in
636 teleost fish," *Journal of Experimental Biology* **66** (1977), 10.1242/jeb.66.1.65.
- 637 Falgout, R., Cleary, A., Jones, J., Chow, E., Henson, V., Baldwin, C., Brown, P., Vassilevski,
638 P., and Yang, U. M., "HYPRE: High Performance Preconditioners," *Users Manual. Version 1*
639 (2010).
- 640 Fish, F. E., "Advantages of aquatic animals as models for bio-inspired drones over present AUV
641 technology," *Bioinspiration and Biomimetics* **15** (2020), 10.1088/1748-3190/ab5a34.
- 642 Floryan, D., Van Buren, T., Rowley, C. W., and Smits, A. J., "Scaling the propulsive performance
643 of heaving and pitching foils," *Journal of Fluid Mechanics* **822** (2017), 10.1017/jfm.2017.302.
- 644 Gazzola, M., Argentina, M., and Mahadevan, L., "Scaling macroscopic aquatic locomotion," *Nature*
645 *Physics* **10** (2014), 10.1038/nphys3078.
- 646 Gazzola, M., Mameau, C., Tchieu, A. A., and Koumoutsakos, P., "Flow Mediated Interactions
647 Between Two Cylinders at Finite Re Numbers," *Physics of Fluids* **24**, 043103 (2012).
- 648 Griffith, B. E., "IBAMR: An adaptive and distributed-memory parallel implementation of the im-
649 mersed boundary method," URL <https://ibamr.github.io/about> (2013).
- 650 Griffith, B. E. and Patankar, N. A., "Immersed Methods for Fluid-Structure Interaction," (2020).
- 651 Grundner, A., Beucler, T., Gentine, P., and Eyring, V., "Data-Driven Equation Discovery of a
652 Cloud Cover Parameterization," *arXiv preprint arXiv:2304.08063* (2023).
- 653 Gungor, A. and Hemmati, A., "The scaling and performance of side-by-side pitching hydrofoils,"
654 *Journal of Fluids and Structures* **104** (2021), 10.1016/j.jfluidstructs.2021.103320.
- 655 Gungor, A., Khalid, M. S. U., and Hemmati, A., "Classification of vortex patterns of oscillating
656 foils in side-by-side configurations," *Journal of Fluid Mechanics* **951**, A37 (2022).
- 657 Gupta, S., Thekkethil, N., Agrawal, A., Hourigan, K., Thompson, M. C., and Sharma, A., "Body-
658 caudal fin fish-inspired self-propulsion study on burst-and-coast and continuous swimming of a
659 hydrofoil model," *Physics of Fluids* **33** (2021), 10.1063/5.0061417.

This is the author's peer reviewed, accepted manuscript. However, the online version of record will be different from this version once it has been copyedited and typeset.

PLEASE CITE THIS ARTICLE AS DOI: 10.1063/5.0155661

Accepted to Phys. Fluids 10.1063/5.0155661

- 660 Hornung, R. D. and Kohn, S. R., "Managing application complexity in the SAMRAI object-
661 oriented framework," *Concurrency and Computation: Practice and Experience* **14** (2002),
662 10.1002/cpe.652.
- 663 Hornung, R. D., Wissink, A. M., and Kohn, S. R., "Managing complex data and geometry in
664 parallel structured AMR applications," *Engineering with Computers* **22** (2006), 10.1007/s00366-
665 006-0038-6.
- 666 Huera-Huarte, F. J., "Propulsive performance of a pair of pitching foils in staggered configura-
667 tions," *Journal of Fluids and Structures* **81** (2018), 10.1016/j.jfluidstructs.2018.04.024.
- 668 Khalid, M. S. U., Wang, J., Akhtar, I., Dong, H., Liu, M., and Hemmati, A., "Why do anguilliform
669 swimmers perform undulation with wavelengths shorter than their bodylengths?" *Physics of*
670 *Fluids* **33** (2021), 10.1063/5.0040473.
- 671 Khalid, M. S. U., Wang, J., Dong, H., and Liu, M., "Flow transitions and mapping for undulating
672 swimmers," *Physical Review Fluids* **5** (2020), 10.1103/PhysRevFluids.5.063104.
- 673 Kirk, B. S., Peterson, J. W., Stogner, R. H., and Carey, G. F., "libMesh : a C++ library for paral-
674 lel adaptive mesh refinement/coarsening simulations," *Engineering with Computers* **22** (2006),
675 10.1007/s00366-006-0049-3.
- 676 Lamb, H., *Hydrodynamics*, 6th ed. (Cambridge University Press, Cambridge, 1932) p. 182.
- 677 Lecheval, V., Jiang, L., Tichit, P., Sire, C., Hemelrijk, C. K., and Theraulaz, G., "Social conformity
678 and propagation of information in collective u-turns of fish schools," *Proceedings of the Royal*
679 *Society B: Biological Sciences* **285** (2018), 10.1098/rspb.2018.0251.
- 680 Li, L., Liu, D., Deng, J., Lutz, M. J., and Xie, G., "Fish can save energy via proprioceptive
681 sensing," *Bioinspiration and Biomimetics* **16** (2021a), 10.1088/1748-3190/ac165e.
- 682 Li, L., Nagy, M., Graving, J. M., Bak-Coleman, J., Xie, G., and Couzin, I. D., "Vortex phase
683 matching as a strategy for schooling in robots and in fish," *Nature Communications* (2020),
684 10.1038/s41467-020-19086-0.
- 685 Li, L., Ravi, S., Xie, G., and Couzin, I. D., "Using a robotic platform to study the influence
686 of relative tailbeat phase on the energetic costs of side-by-side swimming in fish," *Proceed-*
687 *ings of the Royal Society A: Mathematical, Physical and Engineering Sciences* **477** (2021b),
688 10.1098/rspa.2020.0810.
- 689 Li, Y., Wang, H., Li, Y., Ye, H., Zhang, Y., Yin, R., Jia, H., Hou, B., Wang, C., Ding, H., and
690 Others., "Electron transfer rules of minerals under pressure informed by machine learning,"
691 *Nature Communications* **14**, 1815 (2023).

This is the author's peer reviewed, accepted manuscript. However, the online version of record will be different from this version once it has been copyedited and typeset.

PLEASE CITE THIS ARTICLE AS DOI: 10.1063/5.0155661

Accepted to Phys. Fluids 10.1063/5.0155661

- 692 Lin, Z., Bhalla, A. P. S., Griffith, B. E., Sheng, Z., Li, H., Liang, D., and Zhang, Y., "How
693 swimming style and schooling affect the hydrodynamics of two accelerating wavy hydrofoils,"
694 Ocean Engineering **268**, 113314 (2023).
- 695 Lin, Z., Liang, D., and Zhao, M., "Numerical Study of the Interaction Between Two Immersed
696 Cylinders," in *The 12th International Conference on Hydrodynamics* (2016) p. 55.
- 697 Lin, Z., Liang, D., and Zhao, M., "Interaction Between Two Vibrating Cylinders Immersed in
698 Fluid," in *The 27th International Ocean and Polar Engineering Conference* (International Soci-
699 ety of Offshore and Polar Engineers, San Francisco, California, USA, 2017) p. 8.
- 700 Lin, Z., Liang, D., and Zhao, M., "Effects of Damping on Flow-Mediated Interaction Between
701 Two Cylinders," Journal of Fluids Engineering - ASME (2018a), 10.1115/1.4039712.
- 702 Lin, Z., Liang, D., and Zhao, M., "Flow-Mediated Interaction Between a Vibrating Cylinder and an
703 Elastically-Mounted Cylinder," Ocean Engineering (2018b), 10.1016/j.oceaneng.2018.04.019.
- 704 Lin, Z., Liang, D., and Zhao, M., "Effects of Reynolds Number on Flow-Mediated Inter-
705 action between Two Cylinders," Journal of Engineering Mechanics - ASCE **145** (2019),
706 10.1061/(ASCE)EM.1943-7889.0001670.
- 707 Lin, Z., Liang, D., and Zhao, M., "Flow-Mediated Interaction Between a Forced-Oscillating Cylin-
708 der and an Elastically-Mounted Cylinder in Less Regular Regimes," Physics of Fluids (2022).
- 709 Lindsey, C. C., "Form, function, and locomotory habits in fish," in *Fish Physiology*, Vol. 7 (1978).
- 710 Ma, M., Huang, W. X., and Xu, C. X., "A dynamic wall model for large eddy simulation of turbu-
711 lent flow over complex/moving boundaries based on the immersed boundary method," Physics
712 of Fluids **31** (2019), 10.1063/1.5126853.
- 713 Maertens, A. P., Gao, A., and Triantafyllou, M. S., "Optimal undulatory swimming for a single
714 fish-like body and for a pair of interacting swimmers," Journal of Fluid Mechanics **813** (2017),
715 10.1017/jfm.2016.845.
- 716 Maertens, A. P., Triantafyllou, M. S., and Yue, D. K., "Efficiency of fish propulsion," Bioinspira-
717 tion and Biomimetics **10** (2015), 10.1088/1748-3190/10/4/046013.
- 718 Matchev, K. T., Matcheva, K., and Roman, A., "Analytical Modeling of Exoplanet Transit Spec-
719 troscopy with Dimensional Analysis and Symbolic Regression," The Astrophysical Journal **930**,
720 33 (2022).
- 721 Moriche, M., Flores, O., and García-Villalba, M., "Three-dimensional instabilities in the wake
722 of a flapping wing at low Reynolds number," International Journal of Heat and Fluid Flow **62**
723 (2016), 10.1016/j.ijheatfluidflow.2016.06.015.

- 724 Nair, S. and Kanso, E., "Hydrodynamically Coupled Rigid Bodies," *Journal of Fluid Mechanics*
725 **592**, 393–411 (2007).
- 726 Nangia, N., Bale, R., Chen, N., Hanna, Y., and Patankar, N. A., "Optimal specific wavelength for
727 maximum thrust production in undulatory propulsion," *PLoS ONE* **12** (2017a), 10.1371/jour-
728 nal.pone.0179727.
- 729 Nangia, N., Johansen, H., Patankar, N. A., and Bhalla, A. P. S., "A moving control volume ap-
730 proach to computing hydrodynamic forces and torques on immersed bodies," *Journal of Com-
731 putational Physics* **347** (2017b), 10.1016/j.jcp.2017.06.047.
- 732 Nangia, N., Patankar, N. A., and Bhalla, A. P. S., "A DLM immersed boundary method based
733 wave-structure interaction solver for high density ratio multiphase flows," *Journal of Computa-
734 tional Physics* **398** (2019), 10.1016/j.jcp.2019.07.004.
- 735 Ni, J.-Y., Huang, W.-X., and Xu, C.-X., "Mode transition of a coupled rigid–flexible system in a
736 uniform flow," *Physics of Fluids* **35** (2023).
- 737 Pan, Y. and Dong, H., "Computational analysis of hydrodynamic interactions in a high-density fish
738 school," *Physics of Fluids* **32**, 121901 (2020).
- 739 Pan, Y. and Dong, H., "Effects of phase difference on hydrodynamic interactions and wake patterns
740 in high-density fish schools," *Physics of Fluids* **34**, 111902 (2022).
- 741 Partridge, B. L., "Internal dynamics and the interrelations of fish in schools," *Journal of Compar-
742 ative Physiology A* **144** (1981), 10.1007/BF00612563.
- 743 Rosenthal, S. B., Twomey, C. R., Hartnett, A. T., Wu, H. S., and Couzin, I. D., "Revealing the
744 hidden networks of interaction in mobile animal groups allows prediction of complex behavioral
745 contagion," *Proceedings of the National Academy of Sciences of the United States of America*
746 **112** (2015), 10.1073/pnas.1420068112.
- 747 Santo, V. D., Goerig, E., Wainwright, D. K., Akanyeti, O., Liao, J. C., Castro-Santos, T., and
748 Lauder, G. V., "Convergence of undulatory swimming kinematics across a diversity of fishes,"
749 *Proceedings of the National Academy of Sciences of the United States of America* **118** (2021),
750 10.1073/pnas.2113206118.
- 751 Schwalbe, M. A., Boden, A. L., Wise, T. N., and Tytell, E. D., "Red muscle activity in
752 bluegill sunfish *Lepomis macrochirus* during forward accelerations," *Scientific Reports* **9** (2019),
753 10.1038/s41598-019-44409-7.
- 754 Sfakiotakis, M., Lane, D. M., and Davies, J. B. C., "Review of fish swimming modes for aquatic
755 locomotion," *IEEE Journal of Oceanic Engineering* **24** (1999), 10.1109/48.757275.

This is the author's peer reviewed, accepted manuscript. However, the online version of record will be different from this version once it has been copyedited and typeset.

PLEASE CITE THIS ARTICLE AS DOI: 10.1063/5.0155661

Accepted to Phys. Fluids 10.1063/5.0155661

- 756 Shao, X., Pan, D., Deng, J., and Yu, Z., "Hydrodynamic performance of a fishlike undulating foil
757 in the wake of a cylinder," *Physics of Fluids* **22** (2010), 10.1063/1.3504651.
- 758 Shrivastava, M., Malushte, M., Agrawal, A., and Sharma, A., "CFD study on hydrodynamics of
759 three fish-like undulating hydrofoils in side-by-side arrangement," *Lecture Notes in Mechanical*
760 *Engineering* (2017).
- 761 Taylor, G. K., Nudds, R. L., and Thomas, A. L., "Flying and swimming animals cruise at a Strouhal
762 number tuned for high power efficiency," *Nature* **425** (2003), 10.1038/nature02000.
- 763 Thekkethil, N., Sharma, A., and Agrawal, A., "Unified hydrodynamics study for various types
764 of fishes-like undulating rigid hydrofoil in a free stream flow," *Physics of Fluids* **30** (2018),
765 10.1063/1.5041358.
- 766 Thekkethil, N., Sharma, A., and Agrawal, A., "Self-propulsion of fishes-like undulating hydrofoil:
767 A unified kinematics based unsteady hydrodynamics study," *Journal of Fluids and Structures* **93**
768 (2020), 10.1016/j.jfluidstructs.2020.102875.
- 769 Thekkethil, N., Shrivastava, M., Agrawal, A., and Sharma, A., "Effect of wavelength of fish-like
770 undulation of a hydrofoil in a free-stream flow," *Sadhana - Academy Proceedings in Engineering*
771 *Sciences* **42** (2017), 10.1007/s12046-017-0619-7.
- 772 Triantafyllou, M. S., Triantafyllou, G. S., and Gopalkrishnan, R., "Wake mechanics for thrust
773 generation in oscillating foils," *Physics of Fluids A* **3** (1991), 10.1063/1.858173.
- 774 Triantafyllou, M. S., Weymouth, G. D., and Miao, J., "Biomimetic Survival Hydrodynamics and
775 Flow Sensing," *Annual Review of Fluid Mechanics* **48** (2016), 10.1146/annurev-fluid-122414-
776 034329.
- 777 Tytell, E. D., "Kinematics and hydrodynamics of linear acceleration in eels, *Anguilla rostrata*,"
778 *Proceedings of the Royal Society B: Biological Sciences* **271** (2004), 10.1098/rspb.2004.2901.
- 779 Tytell, E. D. and Lauder, G. V., "Hydrodynamics of the escape response in bluegill sunfish, *Lep-*
780 *omis macrochirus*," *Journal of Experimental Biology* **211** (2008), 10.1242/jeb.020917.
- 781 Van Buren, T., Floryan, D., Quinn, D., and Smits, A. J., "Nonsinusoidal gaits for unsteady propul-
782 sion," *Physical Review Fluids* **2** (2017), 10.1103/PhysRevFluids.2.053101.
- 783 Wang, L. H., Xu, C. X., Sung, H. J., and Huang, W. X., "Wall-attached structures over a
784 traveling wavy boundary: Turbulent velocity fluctuations," *Physical Review Fluids* **6** (2021),
785 10.1103/PhysRevFluids.6.034611.
- 786 Webb, P. W., "Form and Function in Fish Swimming," *Scientific American* **251** (1984),
787 10.1038/scientificamerican0784-72.

This is the author's peer reviewed, accepted manuscript. However, the online version of record will be different from this version once it has been copyedited and typeset.

PLEASE CITE THIS ARTICLE AS DOI: 10.1063/5.0155661

Accepted to Phys. Fluids 10.1063/5.0155661

- 788 Wei, C., Hu, Q., Zhang, T., and Zeng, Y., "Passive hydrodynamic interactions in minimal fish
789 schools," *Ocean Engineering* **247** (2022), 10.1016/j.oceaneng.2022.110574.
- 790 Weihs, D., "Hydromechanics of Fish Schooling," *Nature* **241**, 290–291 (1973).
- 791 Yu, Y.-L. and Huang, K.-J., "Scaling law of fish undulatory propulsion," *Physics of Fluids* **33**,
792 61905 (2021).
- 793 Yucel, S. B., Sahin, M., and Unal, M. F., "Propulsive performance of plunging airfoils in biplane
794 configuration," *Physics of Fluids* **34** (2022), 10.1063/5.0083040.
- 795 Zheng, M., Kashimori, Y., Hoshino, O., Fujita, K., and Kambara, T., "Behavior pattern (innate
796 action) of individuals in fish schools generating efficient collective evasion from predation,"
797 *Journal of Theoretical Biology* **235** (2005), 10.1016/j.jtbi.2004.12.025.

798 **Appendix A: Flow structure maps in detail**

799 This section supplements the detailed flow structure maps in the tested parametric space of
800 our present study. Vorticity contours are drawn to illustrate the flow structures at the Reynolds
801 numbers of $Re = 1000 - 2000$, as seen in Fig. 15 to 19. These flow structures can be classified into
802 six types, as exemplified by Fig. 7 and the type distribution is illustrated by Fig. 8, as discussed in
803 Section III C.

This is the author's peer reviewed, accepted manuscript. However, the online version of record will be different from this version once it has been copyedited and typeset.

PLEASE CITE THIS ARTICLE AS DOI: 10.1063/5.0155661

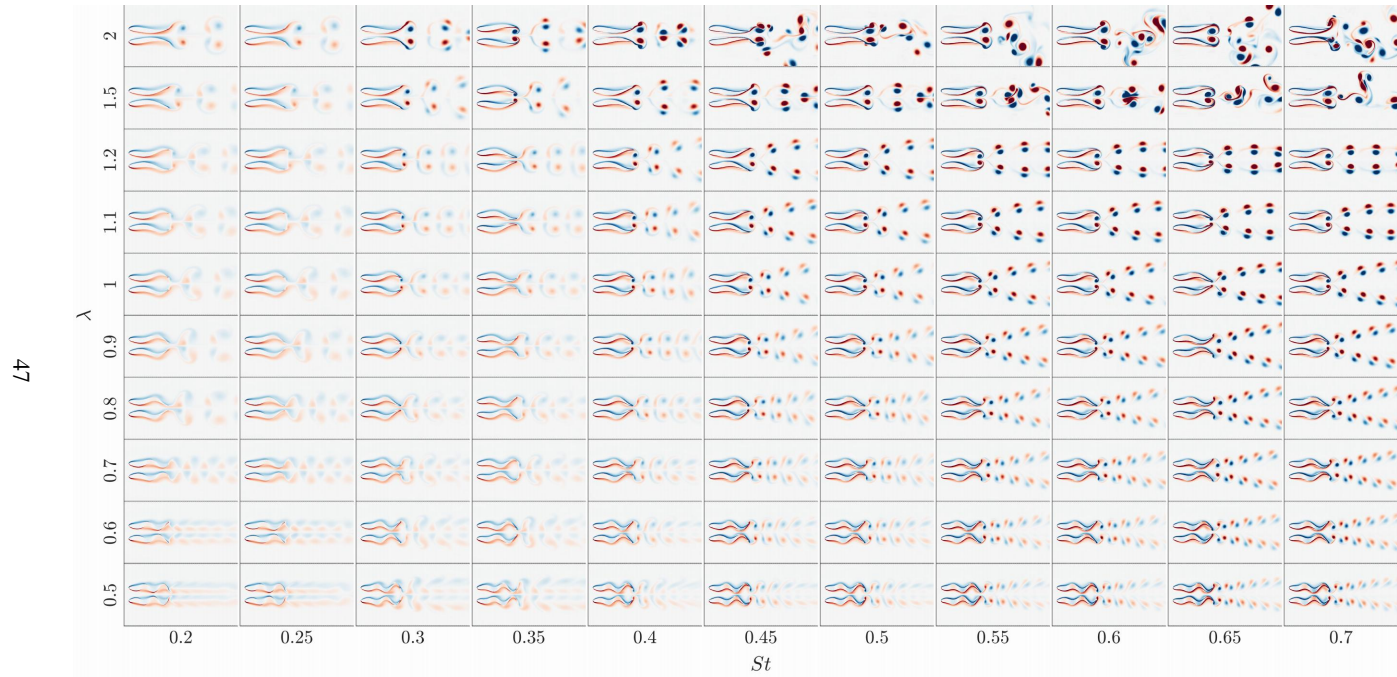


Figure 15. Flow structure visualised by vorticity contours at $Re = 1000$ with $St = 0.2 - 0.7$ and $\lambda = 0.5 - 2$.

This is the author's peer reviewed, accepted manuscript. However, the online version of record will be different from this version once it has been copyedited and typeset.

PLEASE CITE THIS ARTICLE AS DOI: 10.1063/5.0155661

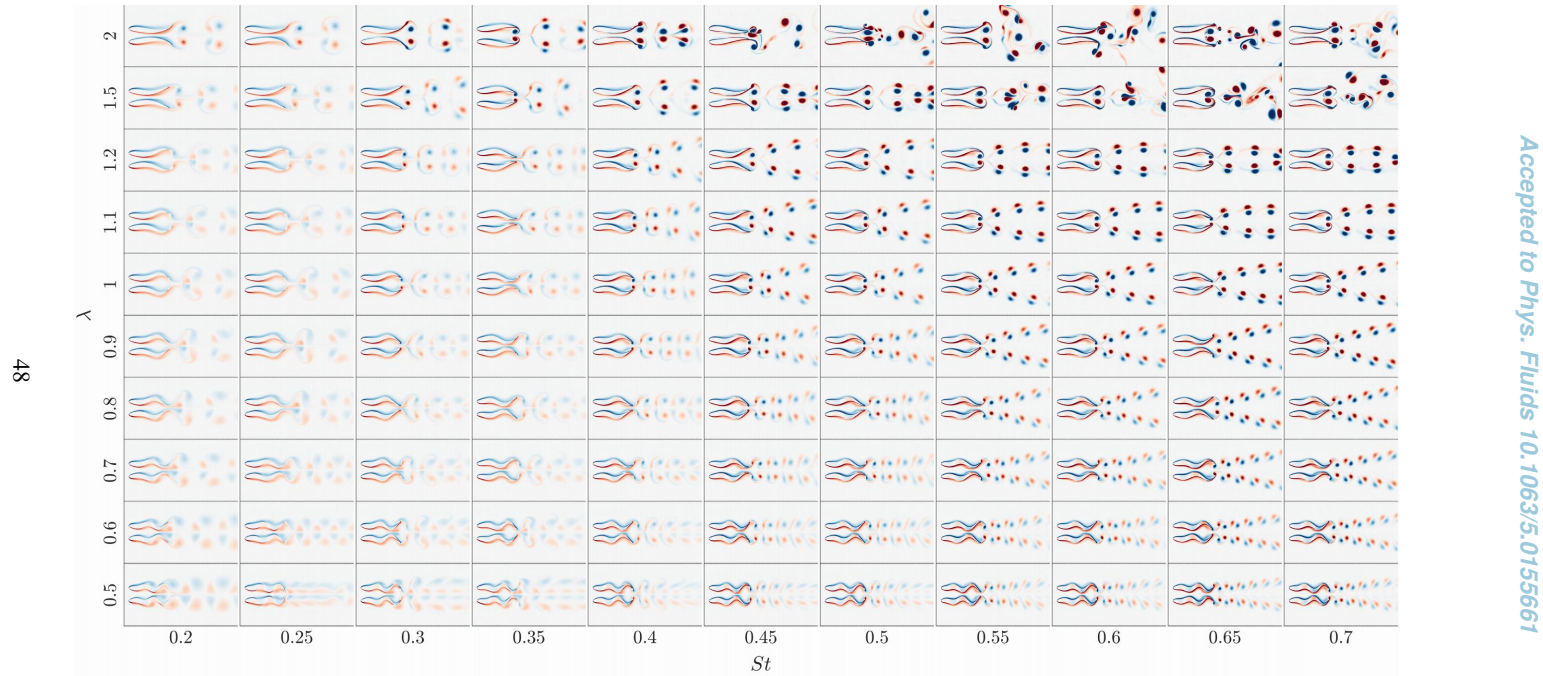


Figure 16. Flow structure visualised by vorticity contours at $Re = 1250$ with $St = 0.2 - 0.7$ and $\lambda = 0.5 - 2$.

This is the author's peer reviewed, accepted manuscript. However, the online version of record will be different from this version once it has been copyedited and typeset.

PLEASE CITE THIS ARTICLE AS DOI: 10.1063/5.0155661

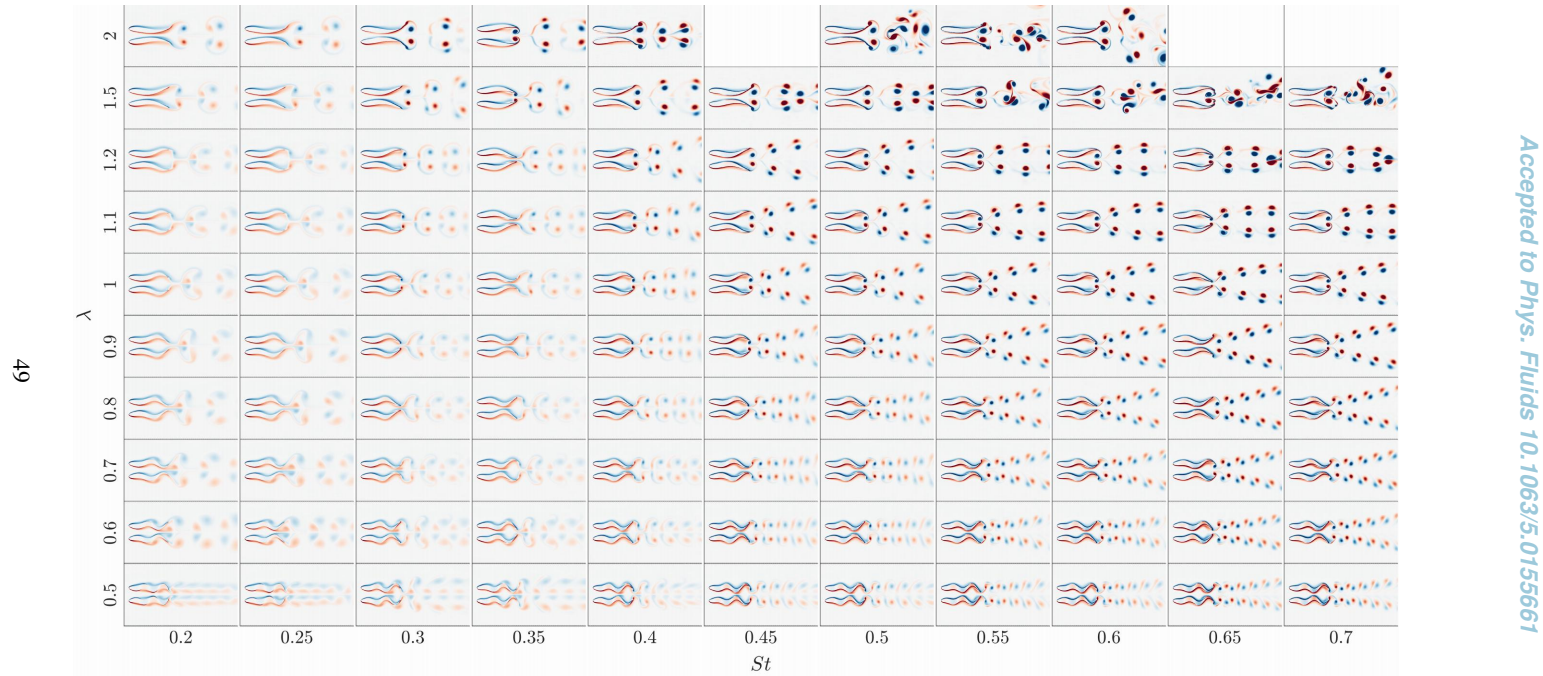


Figure 17. Flow structure visualised by vorticity contours at $Re = 1500$ with $St = 0.2 - 0.7$ and $\lambda = 0.5 - 2$.

This is the author's peer reviewed, accepted manuscript. However, the online version of record will be different from this version once it has been copyedited and typeset.

PLEASE CITE THIS ARTICLE AS DOI: 10.1063/5.0155661

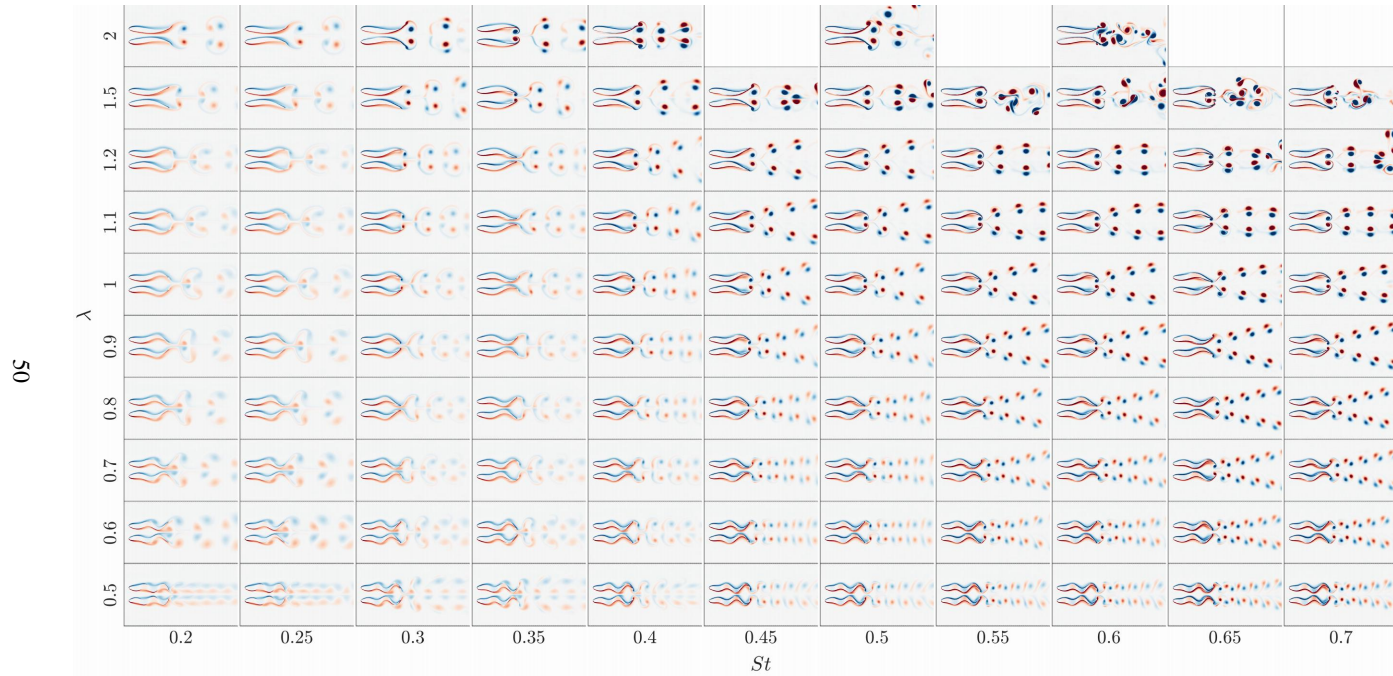


Figure 18. Flow structure visualised by vorticity contours at $Re = 1750$ with $St = 0.2 - 0.7$ and $\lambda = 0.5 - 2$.

This is the author's peer reviewed, accepted manuscript. However, the online version of record will be different from this version once it has been copyedited and typeset.

PLEASE CITE THIS ARTICLE AS DOI: 10.1063/5.0155661

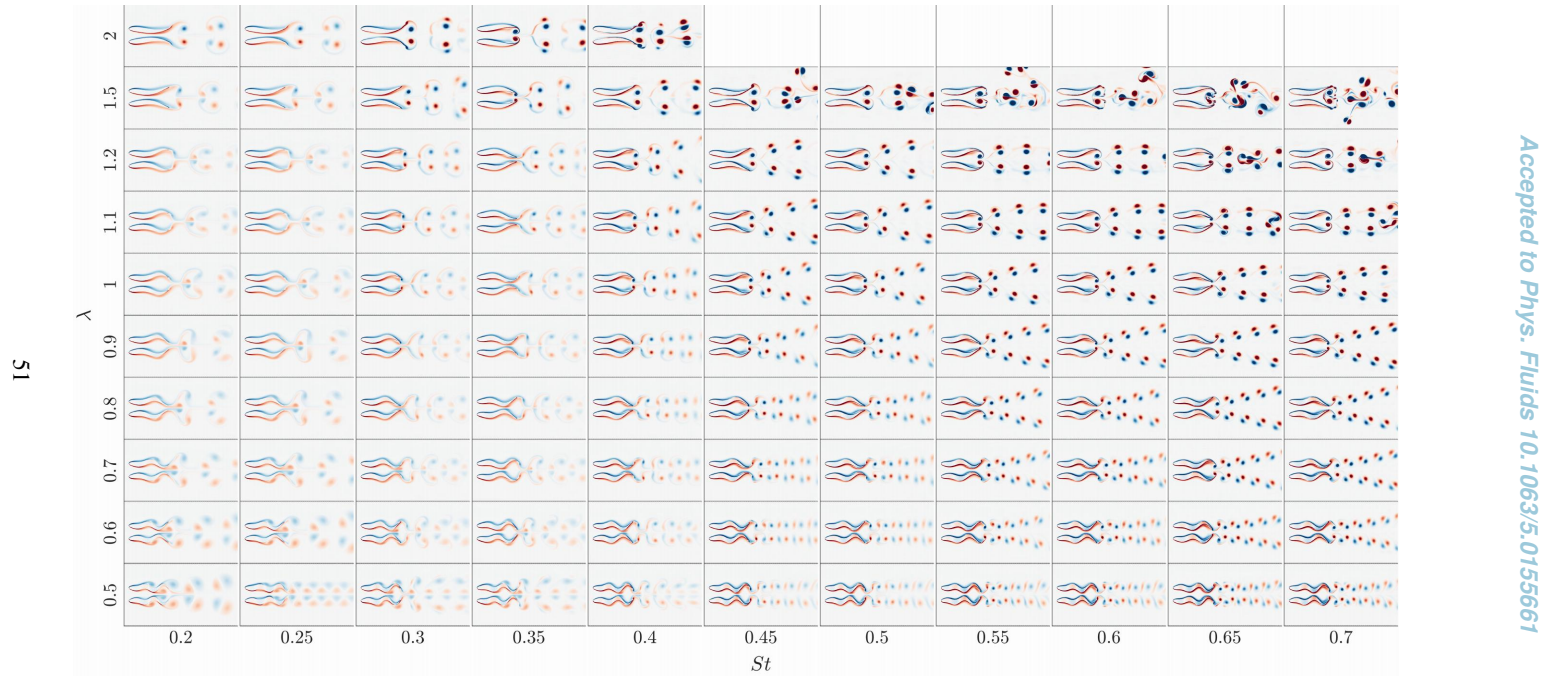


Figure 19. Flow structure visualised by vorticity contours at $Re = 2000$ with $St = 0.2 - 0.7$ and $\lambda = 0.5 - 2$.

804 **Appendix B: Derivation of Thrust Amplification Factor and Metrics for Thrust &** 805 **Propulsive Efficiency**

806 This section expounds on the derivation of the thrust amplification factor and elucidates our
807 choice of metric for propulsive efficiency. The metric for net Froude or propulsive efficiency
808 employed herein is congruent with that used by Akanyeti *et al.* (2017), denoting the efficacy with
809 which the thrust force is generated.

810 The justification for our computation of the thrust amplification factor lies in the following:
811 given a situation where the net average thrust coefficient for a single foil, $\bar{C}_{T,\text{single}}$, converges to
812 zero — that is, in a steady swimming scenario — the denominator of the thrust amplification
813 factor, $\bar{C}_{T,\text{pair}}/\bar{C}_{T,\text{single}}$, would correspondingly converge to zero. This occurrence results in an ex-
814 orbitantly large value for the amplification factor. However, our data-processing procedures duly
815 account for this. In the course of our post-processing computation of the thrust amplification fac-
816 tor $\bar{C}_{T,\text{pair}}/\bar{C}_{T,\text{single}}$ and efficiency amplification factor $\eta_{\text{pair}}/\eta_{\text{single}}$, we calculate the amplification
817 factor only if $\bar{C}_{T,\text{pair}} > 0.01$ and $\bar{C}_{T,\text{single}} > 0.01$ — both of which are larger than a pre-established
818 threshold. If these conditions are not met, the amplification factor is set as zero in the heat maps.
819 The absence of this restriction would have the amplification factor reaching an excessive scale
820 of 10^3 owing to its proximity to zero and numerical discrepancies. The choice of 0.01 ensures a
821 satisfactory distance from zero while considering the potential range of numerical variances.

822 Delving further into specifics, we discerned that $\bar{C}_{T,\text{pair}} = 0.2289$ while $\bar{C}_{T,\text{single}} = 0.0165$. We
823 thus regard the single swimmer *net* thrust $\bar{C}_{T,\text{single}} = 0.0165$ as sufficiently larger than the steady
824 swimming condition $\bar{C}_{T,\text{single}} \approx 0$, especially in comparison to other results, where the net thrust
825 can approach zero as $\bar{C}_{T,\text{single}} = 2.24 \times 10^{-5} \approx 0$.

826 This section also examines the definitions of thrust and efficiency. Our study principally ad-
827 dresses the imbalanced situation of linear acceleration, deviating from the steady swimming con-
828 ditions examined in prior works (Pan and Dong, 2020). Consequently, our chosen metrics are the
829 *net* thrust coefficient and the *net* Froude or propulsive efficiency — that is, the efficiency calculated
830 from net thrust. In the context of this work, the *net* thrust coefficient, $\bar{C}_{T,\text{pair}}$, signifies the net force
831 propelling the swimmer, while the *net* Froude efficiency indicates the proficiency with which the
832 force or acceleration is generated. For an in-depth exploration, we kindly direct the reader to our
833 previous publication which focuses on acceleration Lin *et al.* (2023), where we have extensively
834 justified our chosen metrics.

835 The concept of efficiency is identical between the present paper and that by Dong and Lu
836 (2007). The metric is fundamentally the Froude efficiency derived from net thrust as:

$$837 \quad \eta = \frac{\text{Thrust}_{\text{ave}} \times U}{\text{Power}_{\text{ave}}} = \frac{\bar{C}_T}{\bar{C}_P} \quad (1)$$

838 In their paper "Efficiency of Fish Propulsion", Maertens, Triantafyllou, and Yue (2015) re-
839 viewed numerous extant metrics of "fish swimming efficiency". The "propulsive efficiency"
840 adopted in this paper equates to the "net propulsive efficiency" referenced in Maertens, Triantafyl-
841 lou, and Yue (2015), defined in their work as $\eta = \bar{C}_T / \bar{C}_P$. The optimal "net propulsive efficiency"
842 equates to the minimum energy consumption required to attain a given acceleration. This is dis-
843 tinct from the optimal steady swimming efficiency, which sustains a specific velocity with zero
844 acceleration. Maertens, Triantafyllou, and Yue (2015) proposed a novel metric, quasi-propulsive
845 efficiency, as $\eta = (\bar{C}_T + C_D) / \bar{C}_P$, which incorporates a separately measured drag term. How-
846 ever, we posit that this new metric is better suited for gauging overall swimming performance
847 rather than acceleration performance Maertens, Triantafyllou, and Yue (2015). For more detailed
848 discussions, please refer to the appendix in our previous publication (Lin *et al.*, 2023).

849 Maertens, Gao, and Triantafyllou (2017) employed quasi-propulsive efficiency, where the
850 "thrust" used for calculation is determined by "towing a rigid body in a static flow with a pre-
851 scribed velocity". This methodology circumvents the issue of zero net thrust force and consequent
852 zero efficiency during steady swimming—the central focus of the Maertens, Gao, and Triantafyl-
853 lou (2017) paper. Contrarily, the current manuscript prioritises acceleration over steady swimming
854 conditions, wherein the net force is non-zero. Hence, we compute the propulsive efficiency using
855 net thrust instead of the method used by Maertens, Gao, and Triantafyllou (2017).

856 Pan and Dong (2020) likewise focused on steady swimming. They used *pure* thrust—that
857 is, without considering the drag—rather than *net* thrust, to calculate a modified form of Froude
858 efficiency as $\eta = FU / (FU + P_{\text{wake}})$, where P_{wake} denotes the power in the wake.

859 In summary, the calculation of thrust amplification factor and the chosen efficiency metric of
860 net Froude or propulsive efficiency is apt for investigating the current issue pertaining to linear
861 acceleration.